Skoltech

Skolkovo Institute of Science and Technology

A robot and a computer vision system for disease detection and crop yield estimation in greenhouse monitoring

Doctoral Thesis
by

Ilya Osokin

Doctoral Program in Computational and Data Science and Engineering

Supervisor
Associate Professor, Pavel Osinenko

A robot and a computer vision system for disease detection and crop yield estimation in greenhouse monitoring

by

Ilya Osokin

Monday 28th July, 2025 19:10

Submitted to the Skoltech Center of Research, Entrepreneurship and Innovation
on November 2025, in partial fulfillment of the requirements for the
Doctoral Program in Computational and Data Science and Engineering

Abstract

In short this is the content of my work...

Publications

Main author

1. Skoltech. CEDESK - Concurrent Engineering Data Exchange Skoltech, 2017. URL https://cedesk.github.io/

Co-author

1. Skoltech. CEDESK - Concurrent Engineering Data Exchange Skoltech, 2017. URL https://cedesk.github.io/

Dedicated to Marina.

Acknowledgments

Let me thank to all my supporters ...

Contents

List of Figures

List of Tables

Chapter 1

Introduction

Let me introduce to the topic of my PhD work at Skolkovo Institute of Science and Technology (SK).

1.1 Thesis Structure

The diagram in **??** illustrates the flow of information through the structure of the thesis.

?? - Background Here's the literature review.

?? - Thesis Objectives We define the objectives of our work.

...

?? - Conclusion In the last chapter, we discuss our results obtained ...

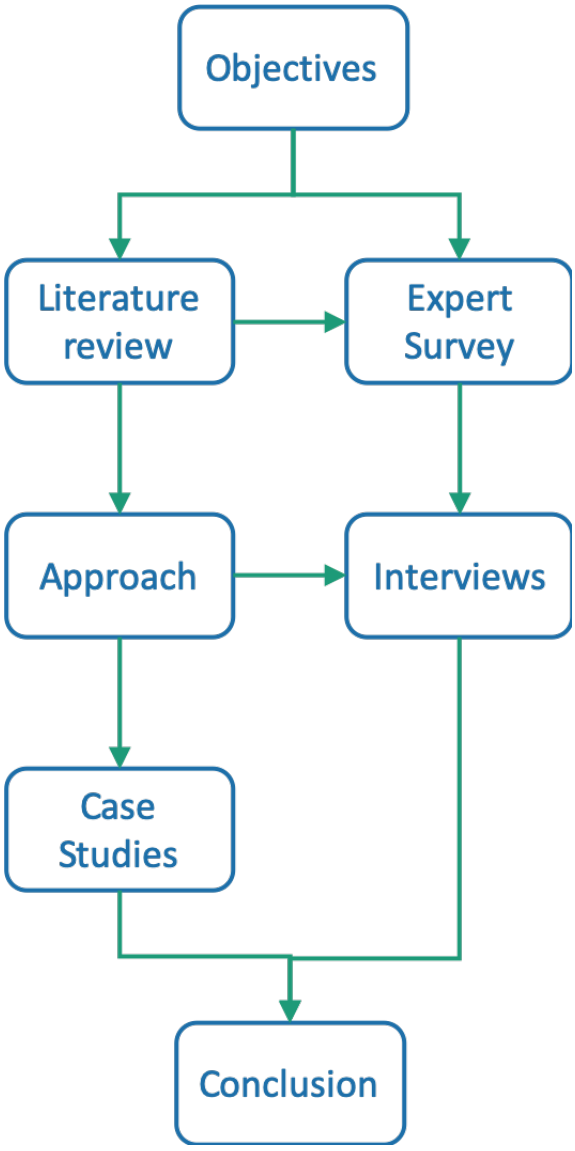

Figure 1-1: Thesis structure

"if I have seen further it is by standing on the shoulders of Giants."

Isaac Newton, 1675

Chapter 2

Background

Here is a comprehensive review of the literature related to the topic of this work.

We inspired our work from **?**. SysML is the reference in this field (**?**) The tools keep evolving (**?**).

Chapter 3

Thesis Objectives

In this chapter we define the goals and derive the specific questions to be addressed in our research.

Chapter 4

Robot

Let me introduce to the topic of my PhD work at Skolkovo Institute of Science and Technology (SK).

4.1 Thesis Structure

The diagram in **??** illustrates the flow of information through the structure of the thesis.

?? - Background Here's the literature review.

?? - Thesis Objectives We define the objectives of our work.

...

?? - Conclusion In the last chapter, we discuss our results obtained ...

Let us describe the main design decisions behind the proposed autonomous platform. First of all the target environment should be considered. It is a greenhouse 300 x 400 m where several hundred lines of tomatoes are growing. In the middle of the greenhouse there is concrete road elevated above the main floor. The tomatoes are growing in alliances perpendicular to this center LA. In order for the robot to be true autonomous it is supposed to have two modes of commotion specifically on the concrete floor and on the rails. While the movement on the rails can be implemented in a straightforward manner,

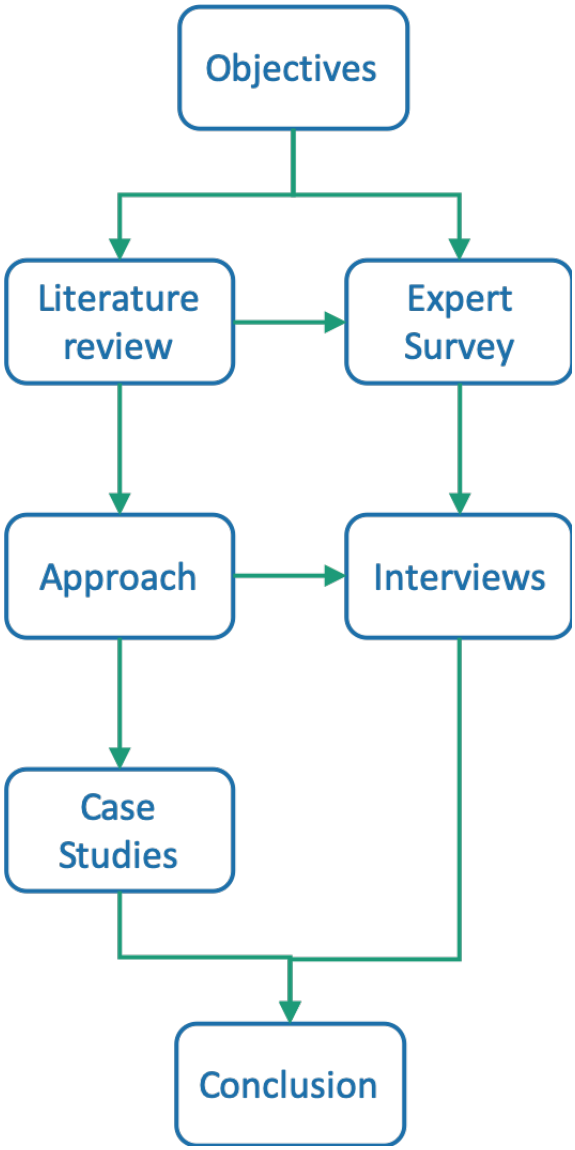

Figure 4-1: Thesis structure

they design decision for the concrete is not as simple. On the one hand with the number of actuators necessary should be kept at minimum. Moreover, any kind of complicated real system will be prone to the elements from the surrounding. The environment in the greenhouse is humid, and there could be grains of sand, dust, or even small puddles of water here and there. On the other hand, the width of the concrete road is approximately 3 m. It allows for convenient to side walking for the personnel and manual movement of the machinery. However, the algorithms that control freely moving, Robert have to be capable of executing, sharp terms and obstacle avoidance maneuvers.

After rigorous consideration and literature review McCannon wheels based system was designed. It is much more mechanically complicated than the regular car like platform with only the front wheels steering, but it allows for the Omni directional motion, as well as turning on the spot. Four wheels were placed at the corners of the robot, which should remain the same during all the modifications. An important factor is this smoothness in the uniformity of the concrete surface that cannot be guaranteed in the unknown environment. Thus an individual suspension module for each of the wheels was designed. Modern greenhouses are standardized, meaning that they have the rails at a specified distance from each other. So the geometrical configuration of the robot was derived from that. The first version of the robot was designed and assembled, which was followed by the real test in a greenhouse during the tomato production. During the testing, it has become clear that despite the specifications, unknown and unpredictable circumstances can appear. One of the main ones was that despite the robot properly feeding in the in between the lines of the tomatoes it was at times, touching the tomato plant parts that were hanging lower than they should be. The integration of an agricultural robot should be performed as smooth as possible, meaning the non-invasive manner and keeping the greenhouse modifications to the bare minimum as well as the workflow there. Thus a decision was made to reduce the width of the robot by integration, the activators inside the wheel itself. With such a modification, the robot has become even more compact minimizing the probability of the contact between it and the plant. The road wheels and the rail wheels are mounted coax keeping the number of the activator is necessary down to only four. The motors that are used in the last third version of the robot are normally used in electric bikes. They are protected from the humidity and dust and are capable of functioning in a wide range of external conditions, including temperature. Moreover, with the current mass of the robot, the perspective velocity and the limited acceleration, they are used under very moderate load, assuring their longevity and reducing the need for maintenance. During the design of the last version of the wheel modules, a model of mechanical wheels

that was found convenient, was reproduced using more rigid type of steel. The wheels from the second version of the Robert broke during the testing, making it necessary to develop a more sturdy version. All in all the last version of the wheel modules can be used on the scope of the agriculture, agricultural applications. They could be mounted to an object with a few modifications, only the mounting surfaces and the necessary wiring. The control boards of the wheels were chosen so that they can carry much heavier loads in terms of the current then the ones that typically appear in the robot. Regarding the main hall of the robot, it is manufactured from the aluminum tubes with square cross-section and planer aluminum elements. In the first version of the robot composite materials were used to manufacture the planer elements. Later they were changed to aluminum. It is heavier, but it provides rigidity to the structure of the robot. Moreover, it lifts the burden of active cooling of the interior of the robot by having a surface area of approximately 2 m^2. Regarding the electrical supply of the Robert lithium batteries were chosen with high energy density, and the voltage that can that the motors can work with without a converter. Six batteries approximately 5 kg each were replaced in the exterior module of the robot. Thus the internal space can be used to accommodate the computer and other equipment. The perspective power consumption of 500 W can be sustained for 12 hours. In order to assure smooth integration of all the equipment to the robot and DCAC converter was installed on board providing 220 V for all the devices, allowing them to be powered by their default power converters. While this solution is excessive in terms of the power consumption, it makes the integration of novel modules easier. The devices on board include the main computing module, which is a laptop with a discrete GPU wi-Fi router, a set of cameras, a power converter in the charger. The charger was chosen, such that it can charge all the batteries in three hours and can be controlled with our S4 185 protocol. This makes it possible, not only to perform the monitoring autonomously, but also charge autonomously. Wi-Fi router is installed on board in order for the robot to be capable of providing its own wireless network for the convenience of the

user. While the greenhouses are often highly automated, they are also often located in remote places that lack sufficient coverage of the Internet providers. Moreover, it could be expensive to provide a wireless network of flow literacy and high bandwidth for all the greenhouse. This was one of the reasons why all the computations are performed on board. The second reason is that with instant on the board computations the result could be obtained instantly. Alternatively, an external server could be installed, but such a solution will require a high band with wireless network, capable of streaming up to six full HD videos simultaneous. With the current developments in the field of mobile computing devices, it is possible to perform the inference of modern neural networks and other algorithms to process data on the board in real time. With the speed of the robot that is acceptable from the safety standpoint and the computational capabilities of an integrated, not integrated discrete GPU the problems of disease, identification, and tomato volume estimation can be solved in real time as the robot drives along the line of tomatoes. The software on Robert is pretty standard in terms of the framework and tools. To 20.0 was used as well as open CV by torch by 3-D Python syphilis plus Ross two. The motor drivers were programmed in C.

robot: - mechanical frame - wheels - electrical subsystem (batteries, motors) - masts - software - cameras

Chapter 5

Volume estimation

Let me introduce to the topic of my PhD work at Skolkovo Institute of Science and Technology (SK).

5.1 Thesis Structure

The diagram in **??** illustrates the flow of information through the structure of the thesis.

?? - Background Here's the literature review.

?? - Thesis Objectives We define the objectives of our work.

...

?? - Conclusion In the last chapter, we discuss our results obtained ...

Abstract. In this work a random sample consensus-based method of second order curve recognition is examined in terms of the dependency of the output quality on the intensity of noise in the input data. Specifically, the recognition method is applied to ellipses. The quality is evaluated the intersection over union between the real ellipse and the predicted one. The results quantitively describe the dependency of the output quality on the characteristics of input data, suggesting deterioration of the model as the data becomes more and more noisy. A series of numerical experiments is conducted on challenging synthetic data. INTRoDUCTION Curve

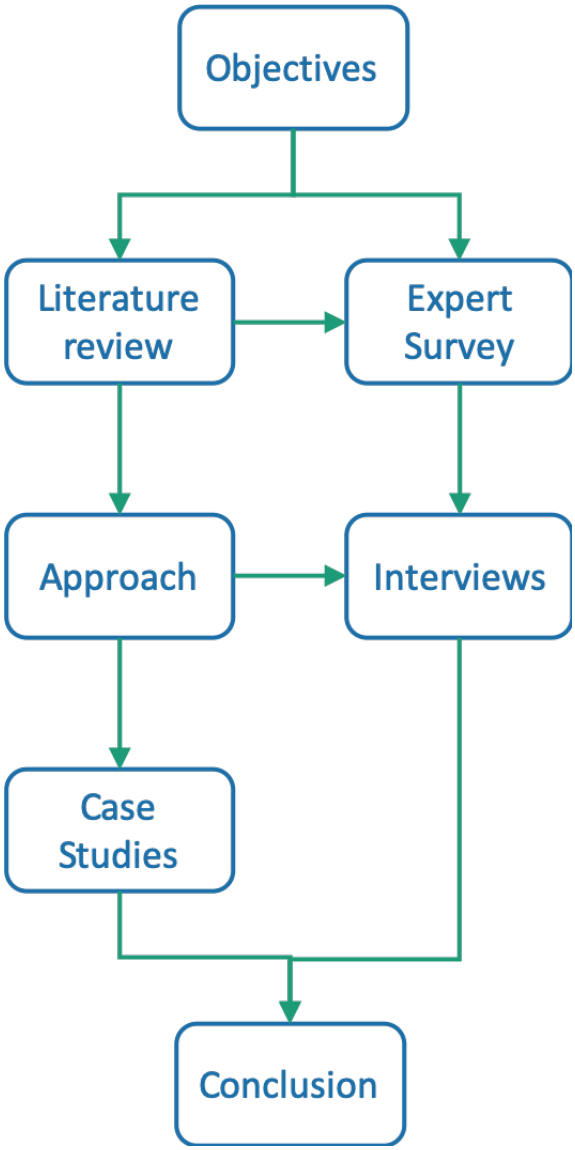

Figure 5-1: Thesis structure

recognition and shape recognition is an important part of many modern industrial applications. In particular, ellipses are used to approximate the section of a tube, human head, and other objects that appear as ellipses [1]. Real-world 3D circles appear as ellipses to a tilted camera, and its parameters provide information about the position, distance and the inclination angle of the said circle.

There is a number of approaches to the shape recognition problem. The most widely used include least squares method, Hough transform and RANdom SAmple Consensus(RANSAC) [2]. Let us briefly cover the main features of these approaches. First of all, least squares method is simple, straightforward, fast, easy to interpret. It

relies on the quadratic error function that is differentiated with respect to the model parameters. It results in a set of equations that could be solved for the values of the parameters that minimize the quadratic error. While this method is widely used, it has certain drawbacks. The main one is that this method lacks robustness to noise. If presented with a data with a small portion of strong outliers, least squares method will incorporate those outliers in the calculation of the optimal model parameters, which significantly degraded the quality of the output model. Consequently, least squares methods cannot be used if significant noise is present.

In the 1960s, when modern computers started to appear in research institutions, a novel approach to data analysis was invented. It was widely adopted, previously being unusable by human workers because of heavy computational burden that should be carried in order for this method to work. This method goes by the name of Hough transform. In contrast to the previously mentioned least squares method, this approach relies on the explicit formation of the discretized parameter space for all the possible models. For such objects as lines the dimensionality of the parameter space is two if these lines exist on the two-dimensional plane. For such objects as circles or parabolas the dimensionality of the parameter space will be equal to three. For such objects as ellipses the dimensionality of the perimeter space will be equal to five.

Hough transform algorithm works as follows. First, a so-called accumulator is created. The dimensionality of this array is equal to the number of independent parameters in the model. It is usually set to be an array with the integer elements. For instance, for circles, it will be a three-dimensional array. Each of the axis will represent x coordinate, y coordinate and the radii of the circle, respectively.

After the accumulator is formed, the main loop begins. It consists of iterative going through all the input data points. For each of them all the possible models are considered that go through that point. A discrete step corresponding to the discretization of the accumulator array is used. For two-dimensional lines a number of the possible models is proportional to Pi over the discretization step. For circles there are two different discretization steps, resulting in the quadratic number of possible models. It could be noted that with the growth of the dimensionality of the

model, the size of the accumulator and the number of iterations grow rapidly. Consequently, for five-dimensional surfaces and curves applying classical Hough transform becomes infeasible.

The input of all these algorithms is a number of two-dimensional points, and the output of the algorithm for ellipses are five parameters, namely two coordinates, two semiaxes, and the rotation angle. The standard way of using ellipse recognition approaches is the following. First, an image is taken with the robot's onboard camera or other imaging device. Second, the image is segmented. Third, the part of the segmentation mask that corresponds to the ellipse is processed in order to decrease the number of pixels in. Finally, all the points are fed into the recognition algorithm.

Random sample consensus is a de-facto standard for a number of computer vision problems, including perspective transform evaluation, 3D reconstruction[3], and pose estimation. A number of works were devoted to the evaluation of the influence of the noise on the output quality[4]. However, RANSAC is not a single algorithm, it is rather a family of algorithms with their performance, speed, complexity, and convergence, depending solely on the class of the models considered[5], [6].

In this work, a systematic approach is taken towards examining the performance of the random sample consensus approach in application to a specific problem of second order curse fitting. The contributions of this work are as follows. First, a simple, self-contained implementation of RANSAC for ellipses is created. Second, a variety of synthetic datasets is generated. Third, a number of numerical experiments are conducted with their results being measured in terms of intersection over union, ellipse parameter correspondence, and area error. Fourth, the dependency of the quality of the output model on the characteristics of the input data are explained. All the code is implemented in Python programming language. MATERials and methods Baseline RANSAC

Let us describe the classical RANSAC algorithm, as per paper by Fischler and Bolles [1]. It was previously mentioned, that least squares suffer from sensitivity to outliers, and Hough transform from the rapid growth of the accumulator size. This is where random sample consensus-based algorithms could be used. In contrast to

the Hough transform, where all the parameter space is considered explicitly, random sample consensus relies on the chosen models from all the possible ones from the perimeter space, thus saving memory. At the same time, in contrast to the least squares methods, random sample consensus is not obliged to take into account all the points of the input data. It relies on the sampling of a number of subset of data. For each subset, a separate model is created. The number of the points in this subset has to be such that it determines a single unique model for lines. It will be two points for a line, and for ellipse it will be five points. After the model is obtained, it is calculated how many of the input data points are described by the model.

This notion of how the data points are described by the model is in itself a variety of different approaches. The first way to tell if the data point is described by a model is to measure the distance from this point to this model, and the second way of doing this relies on the so-called algebra distance. Considering a case of an ellipse, the equation describing it is a second-order equation with two independent variables. If the left side of this equation is considered as a polynomial, the value of this polynomial is zero on the ellipse and not zero inside and outside. The value of the polynomial on the data point could be considered as a distance from the point to the model. There are also alternative approaches to the measurement of the distance from the point to the model. In particular, there is a mixture of the geometrical distance, and the distance measured along the semiaxes of the ellipsoid in the paper [7].

There are also ways to count the fitness of the model for the dataset. After the distances are obtained with one of the methods described above, a single scalar metric should be calculated. It could be a sum of indicator functions. If the distance from the point to the model is below a certain threshold, the point is considered to be fit for the model. The best model among the same ones is the one that has the biggest number of inliers. However, there are alternative approaches to counting the fitness of the model for the data. For instance, monotonous decreasing function could be used as a weight function instead of the threshold function, such as the exponential of minus distance from the point to the model.

Random sample consensus algorithm is inherently stochastic. It relies on the random generator, and also if part of the input data is outliers, it will produce a reasonable output only with a certain probability. Let us briefly cover the question of the numerical evaluation of this probability. Let n be the number of the input points and be the share of the non-noise data points, k be the number of points that describe a unique model, and P be the desired probability of obtaining an output model that corresponds to the real object. The probability of sampling a single point that is an inlier is . The probability of sampling k points that are all inliers is . The probability of sampling at least one outlier point is equal to . Sampling even a single outlier point will result in the incorrect model. If m subsets of points are sampled, the probability of all of them containing at least one outlier is equal to . This formula could be equated to , which is the acceptable probability of not producing a feasible model: . Taking logarithm from both sides yields the following result for the number of sampling iterations:

It is evident that as the desired probability grows, the number of the necessary samplings increases.

Implementation for second-order curves

Each of the data points of the form is transformed into a vector

Representing the parameters of the ellipse equation in the form of

allows to rewrite the equation as with an arbitrary scale parameter F set to 1. Five such equations for a system of equations with a unique solution for the ellipse parameters if the points are in non-degenerate configuration. Finally, the center, semiaxes and the rotation angle are obtained, following [8].

Experimental results A number of experiments were conducted. The points of the ellipse were corrupted by additive normal noise with increasing variance. The results of the first series of experiments are presented in the Figure 1(a). As the variance of the noise becomes comparable to the size of the ellipse, the intersection over union becomes unacceptably small for the real-world scenarios.

The second result is presented in the Figure 1(b). A comparison is made between the performance of the algorithm on the same data, but with different number of iterations. It could be noted that while the overall trend of the quality decrease

is evident in all the curves, the orange and green curves (that correspond to 50 and 500 iterations) have lower decrease rate. Moreover, the difference between the performance with 50 and 500 iterations is not significant.

(a) (b)

Figure 1. For each noise level, a number of random sets of data were generated, and the variances were calculated. A clear trend with the decrease in the Intersection over Union can be seen as the ratio between the noise variance and the major semiaxes of the ellipse grows.

Table 1 presents the comparison of the performance of the algorithm under different noise and with changing number of iterations. It could be noted that first, the quality decreases as the noise becomes heavier, and second, the quality improves with the increase in the number of iterations. An important finding is that the difference between 5 iterations and 50 is much more significant than the difference between 50 and 500 iterations. TABLE 1. The values of the Intersection over Union between the real ellipse and the predicted one for the noise of different severity (from 0.3 of maximal amplitude to 0.8). Iterations number Noise 0.3 Noise 0.5 Noise 0.8 5 0.403 0.219 0.174 50 0.499 0.450 0.314 500 0.550 0.487 0.339 CONCLUSION In this work the influence of noise on the quality of the output of RANSAC method was examined. This method was applied to the problem of second-order curve recognition, specifically an ellipse. RANSAC for ellipses was implemented in Python. It relies on the representation of the input data as zero, first and second-order monomials. It follows the standard RANSAC pipeline with inliers being counted by a binary threshold. A set of synthetical noisy data was generated. A number of experiments on was conducted in order to evaluate the influence of that noise on the quality of the output. The results suggest that the increase of the number of iterations leads to diminishing returns in quality. Consequently, it becomes less and less reasonable to allocate more computational resources as the convergence is being reached. Furthermore, the dependency of the output metric on the noise intensity was obtained in a series of tests with increasing noise. It suggests that the quality in terms of IoU drops significantly as the noise variance approaches the order of the size of the ellipse's semiaxes.

References 1. M. Han, J. Kan, Y. Wang, Ellipsoid fitting using variable sample consensus and two-ellipsoid-bounding-counting for locating Lingwu long Jujubes in a natural environment, IEEE Access, 2019 2. M. Fischler, R. Bolles, Random sample consensus: a paradigm for model fitting with applications to image analysis and automated cartography, CACM, 1981 3. I. Nyalala, C. Okinda, L. Nyalala, N. Makange, Q. Chao, L. Chao, K. Yousaf, K. Chen, Tomato volume and mass estimation using computer vision and machine learning algorithms: Cherry tomato model, Journal of Food Engineering, 2019 4. E. Rodriguez, D. Skarecky, N. Narula, T. E. Ahlering, Prostate volume estimation using the ellipsoid formula consistently underestimates actual gland size, The Journal of urology, 179(2):501–503, 2008. 5. J. Yu, H. Zheng, S. R. Kulkarni, H. Vincent Poor, Outlier elimination for robust ellipse and ellipsoid fitting, In 2009 3rd IEEE International Workshop on Computational Advances in Multi-Sensor Adaptive Processing (CAMSAP), pages 33–36. IEEE, 2009. 6. M. Ghahremani, K. Williams, F. Corke, B. Tiddeman, Y. Liu, X. Wang, J. H. Doonan, Direct and accurate feature extraction from 3d point clouds of plants using ransac, Computers and Electronics in Agriculture, 187:106240, August 2021 7. M. Han, J. Kan, G. Yang, X. Li, Robust Ellipsoid Fitting Using Combination of Axial and Sampson Distances, IEEE Transactions on Instrumentation and Measurement, 2023 8. P. Abbott, On the Perimeter of an Ellipse, Mathematica, pp. 172-185, 2009.

Abstract

Random sample consensus-based algorithm (RANSAC) is one of the standard approaches in the field of robust estimation of parametric objects. There are numerous versions of RANSAC that are tailored to specific problems such as homography estimation, point cloud registration, plane estimation and others. On the other hand, numerous attempts were made towards the development of modifications of RANSAC that are extremely robust to noise or highly efficient in terms of the computational demands. However, the general premise of these approaches remains all the same: instead of trying to fit a single model to all the data, a number of small models is produced and evaluated in terms of their ability to describe the data. In this work, an empirical study is carried out that is purposely limited to a specific application of RANSAC. Particularly, the dependency of the output quality on the noise is examined for the quadric surface evaluation. The data was presented in the form of 3D point clouds. A method for synthetic data generation was developed, allowing to

mimic the geometric principles of the point cloud formation. The dependency of the error on the noise was examined on the synthetic point clouds. Finally, numerical experiments on real point clouds were carried out in the agricultural setting. The code can be found in the repository https://github.com/aidagroup/SCUF/ and the proposed method can be used as a module https://pypi.org/project/scuf/.

5.2 Introduction

The ellipsoid identification problem widely arises as a part of modern computer vision in a variety of applications, including agricultural **?** **?**, medical **?**, robotics **?**, and environmental reconstruction **?**.

The real-world setting is often associated with noise in the sensor output, which naturally leads to the demand for robust algorithms for obtaining ellipsoids. Compared to Least Squares, RANSAC demonstrates superior robustness to outliers. RANSAC-based approaches are often used under challenging circumstances, see **?**. With these methods it is possible to solve problems where parts of the data directly contradict the resultant hypothesis, which is often the case with imperfect feature correspondence in vision-related problems. Despite these difficulties RANSAC allows for precise and robust two-view image correspondence **?** **?** and pose estimation **?**.

However, there are certain shortcomings to this approach. First, it is inherently stochastic, lacking reproducibility. Second, looping through the whole set of input data multiple times can be time-consuming. Third, increasing the number of iterations gives diminishing returns in terms of the output quality. Fourth, there is a number of hyperparameters in RANSAC, particularly the threshold value for inlier counting (see Subsection **??** for details) and the assumed fraction of inliers. Both of them have to be tuned manually, and if chosen improperly, can lead to degradation in quality. Fifth, increase in the noise level leads to exponential growth in the number of necessary iterations **?**. Sixth, as the complexity of the parametric model grows, the number of iterations necessary also increases. For line extraction **?** it is enough to sample two points from the data and solve small linear system, but for more complex objects like quadric surfaces the number of the equations in the

system grows to 9 **?**.

A lot of work was done in order to address these issues since the publication of the original work **?**. There are numerous works that are aimed at extending the applicability of RANSAC **?**. One of the possible approaches relies on sampling a set of points with the number that exceeds the minimal necessary **?** in contrast to the baseline RANSAC.

Another extension of the method is Differentiable RANSAC **?**. It relies on the shift towards gradient-based optimization instead of grid search in standard RANSAC.

In order to optimize the number of iterations, Variable Sample Consensus (VARSAC) was proposed **?**.

In the last years a number of works were concerned with adding adaptiveness to RANSAC, for instance by iteratively updating the output hypothesis considering residuals from the previous iterations **?**.

There are works devoted to the evaluation of the influence of the noise on the RANSAC output for certain problems, such as plane estimation **?**. However, none can be found that focus specifically on the quadric surfaces, that is a specific case in the domain of all the RANSAC applications. First, the number of the parameters needed to describe a unique ellipsoid is 9, which is signifinactly more than for a line or a circle, thus leading to a small probability of sampling a subset of points that do not contain outliers. Second, a conventional way of measuing the distance from the surface to the data point is not geometric, but algebraic, meaning the value of the polynomial that defines the surface. In summary, this work is a case study of the application of the classical baseline RANSAC to a specific problem, that is supposed to serve as an estimate of what could be expected of RANSAC-based algorithms in such applications.

The contributions of this paper are as follows:

- A set of synthetic data was generated with ray tracing.
- A real dataset of 3D point clouds was collected in an environment emulating agricultural setting.

- The dataset was marked.
- RANSAC for quadrics was implemented in Python.
- Mutual distributions between the model quality and the inlier number were obtained.
- The dependency of the output quality on the number of iterations was assessed.
- The distribution of the algebraic distance between the sufrace and the data points was obtained.
- The dependency of the volume error on the distance from the camera to the object and on the number of algorithm iterations was assessed.

The rest of the paper is organized as follows.

First, the baseline RANSAC algorithm is described. Second, an ellipsoid extraction method is derived. After that, synthetic data generation algorithm is given with an approach that mimics the way in which the real point cloud data is obtained. Then the real data obtainment and analysis is described. Finally, the experimental results and their interpretations are presented.

5.3 RANSAC for quadric surfaces

5.3.1 Standard RANSAC algorithm

Let us first briefly describe the RANSAC algorithm according to **?**.

RANSAC is a well-known algorithm for obtaining parametric objects in the presence of noise. Unlike methods such as least squares that fit a single model to all the data, including outliers, RANSAC generates multiple models based on small random subsets of data. This increases the probability of selecting points and models belonging to the real object.

RANSAC algorithm for ellipsoids consists of the following steps:

1. **Sampling a random subset of data points.** The size of the subset is chosen in such a way that a unique model can be precisely fitted to it. For ellipsoids 9 points are required.

2. **Fitting the model to the selected subset.** An ellipsoid can be represented as a set of points satisfying the equation in the form of $p_1x^2+p_2y^2+\cdots+p_9z = 1$. With the aforementioned 9 points a system of linear equations is formed, that is solved with standard linear algebra.

3. **Checking the model.** Since there are multiple types of quadric surfaces other than real ellipsoid, a number of additional conditions are checked, specifically the correct signs of certain invariants **?**.

4. **Assessment of the model quality.** The fitness of the model is the numerical metric of how well it represents the entire point cloud. This assessment is performed by counting the number of points that lie close to the surface of the ellipsoid model. To determine this proximity, a threshold-based point counting is performed based on the algebraic distance between the points and the predicted surface. Here the simplest approach to evaluation is used, that was proposed in the classical work of Fischler and Bolles **?**.

5. **Iterative search.** Steps 1-3 are repeated a number of times, and the best model is chosen by the criteria of the number of well-represented points.

The detailed pseudocode is given in Algorithm **??**.

5.3.2 Quadric surface parameters obtainment

Now let us describe the ellipsoid model extraction, that is performed at each step of RANSAC, generally following**?**.

The proof will begin with an ellipse in the XY-plane and then be extended to the ellipsoid.

First, consider a set of points on the unit circle, P_c:

$$P_c = \{r_c \in \mathbb{R}^2 \mid r_c^T r_c = 1\}. \tag{1}$$

Algorithm 1: RANSAC algorithm description

Input: 3D points, k (number of points that uniquely define a model), filtering criteria (restrictions on acceptable ellipsoids), iterations number, inlier threshold

Output: ellipsoid model

Result: quadric polynomial, center coordinates, radii, orientation

1. Points sampling;

points_samples = [];

for $i \leftarrow 0$ **to** *iterations number* 1 **do**

  Randomly select a subset of k points. Save the subset into an array *points_samples*;

2. Estimation of the parameters of the models;

hypotheses = [];

for $i \leftarrow 0$ **to** *iterations number* 1 **do**

  For each subset of points from *points_samples* form a $k \times k$ system and solve it; Calculate invariants

  if *invariants have proper signs* **then**

    Save the corresponding polynomial P, matrices and parameters M_i into an array of *hypotheses*;

  else

    Continue;

3. Model checking and validation;

$Models$ = [];

m = size(*hypotheses*) **for** $i \leftarrow 0$ **to** m 1 **do**

  if M_i *semi-axes from hypotheses satisfy the conditions on size and semiaxis ratio* **then**

    Save $Model_i$ to array $Models$

  else

    Continue;

4. Inliers analysis;

Loop through the models and find i such that the model $Model_i$ maximises $\sum_{j=1}^{m} \mathbb{I}(|P_i(x_j)| < \text{threshold})$, where $P_i(x_j)$ is the value of the polynomial number i on the data point number j.

Return this model.

Let us introduce

$$\begin{aligned} &t \in \mathbb{R}^2 \ - \ \text{translation vector}, \\ &s \in \mathbb{R}^2 \ - \ \text{scale vector}, \\ &\alpha \in [0, 2\pi) \ - \ \text{rotation angle}. \end{aligned} \tag{2}$$

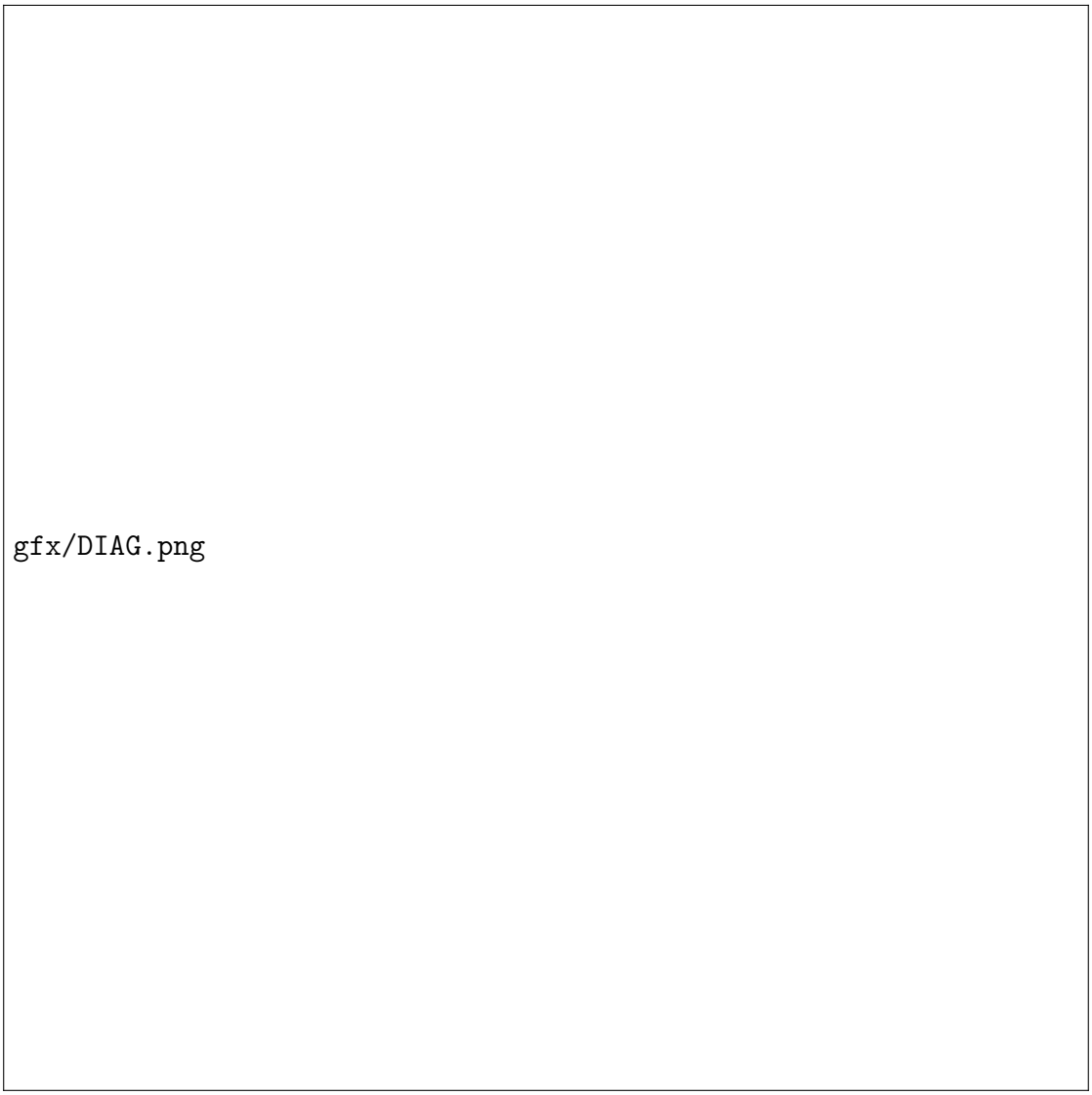

Figure 5-2: The scheme of the experimental setup. First, an RGB and depth-images are taken. Second, a color-based filter is applied to the RGB image and the corresponding parts of the point cloud are cut. Finally, RANSAC if applied to each of the objects and the results are evaluated against the markup.

With the matrix operations it is possible to transform unit circle into an arbitrary ellipse.

Let us unwrap the full form of these matrices.

$$S = \begin{pmatrix} s_1 & 0 \\ 0 & s_2 \end{pmatrix} \quad \begin{array}{l} - \text{ scale matrix, where} \\ s_1 \text{ and } s_2 \text{ are parame-} \\ \text{ters of scale vector } \mathbf{s}, \end{array}$$

$$R = \begin{pmatrix} \cos(\alpha) & -\sin(\alpha) \\ \sin(\alpha) & \cos(\alpha) \end{pmatrix} \quad - \text{ rotation matrix.} \tag{3}$$

Let P_e be the points of the ellipse. Scaling, rotation and translation of the unit circle yields

$$P_e = \{RSr_c + t \mid r_c \in P_c\}. \tag{4}$$

From (1) a matrix equation of the ellipse can be obtained. For $r \in P_e$ the equation of the ellipse takes form of

$$(r-t)^T[R^{-1}]^T[S^{-1}]^T S^{-1}R^{-1}(r-t) = 1. \tag{5}$$

Since R is an orthogonal matrix and S is a diagonal matrix, $R^{-1} = R^T$ and $S^T = S$.

$$(r^T - t^T)RS^{-2}R^T(r-t) = 1. \tag{6}$$

Let us introduce $V = RS^{-2}R^T$ for convenience. Inserting this into equation (6) yields:

$$r^T V r - 2t^T V r + t^T V t = 1. \tag{7}$$

Let us also introduce vector $v^T = t^T V$ and scalar $v_0 = t^T V t$.

$$r^T \left[\frac{V}{v_0 - 1} \right] r - 2 \left[\frac{v^T}{v_0 - 1} \right] r + 1 = 0. \tag{8}$$

Finally, let us define a matrix $M = \frac{V}{v_0 - 1}$ and a vector $m^T = \frac{v^T}{v_0 - 1}$. Now it is possible to formulate the general matrix equation of an ellipse as follows:

$$r^T M r - 2 m^T r + 1 = 0. \tag{9}$$

From this equation all the parameters needed to describe an arbitrary n-dimensional ellipsoid can be extracted, specifically translation, rotation and scaling.

Let us evaluate M^{-1} first.

$$M^{-1} = \left[\frac{V}{v_0 - 1} \right]^{-1} = (v_0 - 1) V^{-1} = (v_0 - 1) R S^2 R^T. \tag{10}$$

It could be observed that

$$t = M^{-1} m. \tag{11}$$

Considering the eigendecomposition of M yields

$$\begin{aligned} M = \frac{1}{v_0 - 1} V = \frac{1}{v_0 - 1} R S^{-2} R^T = \\ R \left[\frac{1}{v_0 - 1} S^{-2} \right] R^T = Q \Lambda Q^{-1}. \end{aligned} \tag{12}$$

From (12) it could be seen that the eigenvectors matrix of M is exactly the rotation matrix R.

$$R = Q. \tag{13}$$

Moreover, the matrix of the eigenvalues M and S are diagonal matrices:

$$\Lambda = \frac{1}{v_0 - 1} S^{-2}. \tag{14}$$

Thus, it becomes possible to extract the scale matrix S from the eigenvalues matrix Λ.

Scale matrix S consists of squeezes and stretches along orthogonal axes of the ellipse, or just radii. Each eigenvalue can be presented as

$$\lambda_i = \frac{1}{v_0 - 1} s_i^{-2}. \tag{15}$$

In order to extract the radii, it is necessary to find v_0 first. Since

$$v^T V^{-1} v = v_0. \tag{16}$$

And

$$m^T M^{-1} m = \frac{1}{v_0 - 1} v_0. \tag{17}$$

Finally, an expression for s_i can be found.

$$s_i = \sqrt{\frac{m^T M^{-1} m - 1}{\lambda_i}}. \tag{18}$$

The solution holds with respect to the permutations of the axes of the ellipse.

5.4 Data

Three sets of data were used in the numerical experiments. The first are the synthetic ellipsoids generated with a naive straightforward method, see subsection **??**. The second are the data generated with the ray emulation approach, see subsection **??**. Finally, the third is the real data recorded with Intel RealSense D435i camera, see subsection **??**. Let us describe these sets of data.

5.4.1 Naive synthetic ellipsoids generation

The first dataset contains points evenly distributed on the surface of ideal ellipsoids. The ellipsoid is described by its center, semiaxes, and rotation. After specifying those, a point cloud is created, consisting of points on the surface of the ellipsoid. These data were used as the simplest possible to evaluate the algorithm's performance. As one might expect, the error on clear data was precisely zero, so data with additive normal noise was considered as well, see Table **??** and Table **??**.

The point clouds that are generated this way are different from the real ones due to the non-uniform surface coverage in the real data and only partial visibility to the real camera.

5.4.2 Ray emulation-based synthetic data generation

Thus, an alternative approach was taken with a proper geometrical model of the camera. Stereoscopic vision, either active or passive, relies on the difference in the appearance of the same objects from two distinct viewpoints. Their correspondence allows for the reconstruction of the depth in the scene. It should be noted that with such an approach the ellipsoid is covered with points not uniformly, see Figure **??**. An explicit geometrical model was used to obtain data that closely resembles the real point clouds.

According to the used model, a tomato can be represented as an ellipsoid. Hence, the point cloud obtained from a real tomato can be approximated as the point cloud of an ideal ellipsoid. In this section, the process of image formation is considered.

Figure 5-3: Scheme of the ray tracing-based approach to point cloud generation. On the left a focus of the camera is presented, the red grid in the middle is the camera matrix, and the rays casted from through it intersect with the surface of the ellipsoid in the points marked with cyan triangles.

The leftmost violet point in Figure **??** represents the focal center of the camera, while the red points correspond to the light-sensitive pixels of the camera matrix. A line between the blue and red points visualizes a beam of light reflected from the ellipsoid that intersects with the camera matrix. Extending this line to intersect with the ellipsoid yields a point in the point cloud (cyan triangles). Thus, the problem of finding the intersection of a line formed by two points with the ellipsoid needs to be addressed.

Let us consider an ellipsoid defined by S (scale matrix), R (rotation matrix), and t (translation vector), along with a line formed by points A and B.

First, let us transform the ellipsoid so that it becomes a unit sphere at the origin in order to simplify the problem. The points A and B will be transformed as follows:

$$\begin{aligned} A' &= S^{-1}R^T(A - t), \\ B' &= S^{-1}R^T(B - t). \end{aligned} \tag{19}$$

The direction vector defining the light beam line in the new coordinates can be found as:

$$a = \frac{A' - B'}{\|A' - B'\|}. \tag{20}$$

The solution for the line-sphere intersection yields two points P_1 and P_2, that can be found according to the subsequent computational steps derived from solving a quadratic equation, if $\Delta \geq 0$.

$$\begin{aligned} \Delta &= (a^T A')^2 - (A')^T A + 1, \\ C' &= A' - a^T A' a, \\ P_1' &= C' - a\sqrt{\Delta}, \\ P_2' &= C' + a\sqrt{\Delta}, \\ P_1 &= RS(P_1' + t), \\ P_2 &= RS(P_2' + t). \end{aligned} \tag{21}$$

By repeating this algorithm for each red point representing pixels, an array of points that lie on the ellipsoid is formed, see Figure **??**. After that the noise is added into the data, see Figure **??**. The amplitude of noise was chosen in accordance with the real data.

5.4.3 Real data

The point cloud in the Figure **??** is from the real part of the dataset. These point clouds are a challenging piece of data. Tomatoes are described by an ellipsoid model only in a certain approximation, varying from fruit to fruit and from strain to strain. It means that even the best possible fit will result in a certain non-zero error.

Moreover, the real noise cannot be approximated by the normal noise model. In

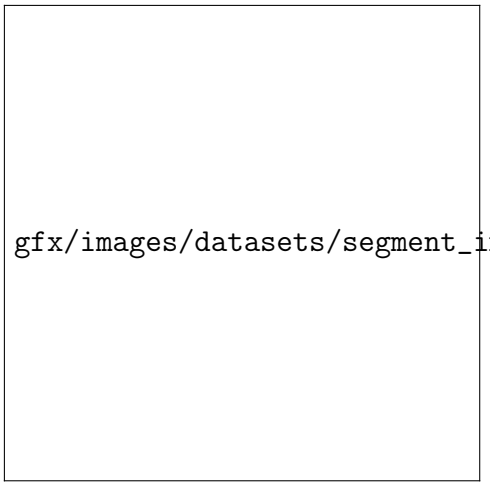

(a) Example of a point cloud of an ellipsoid segment without noise

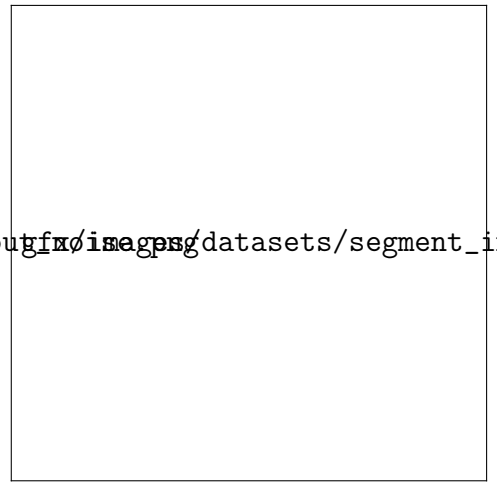

(b) Example of a point cloud of an ellipsoid segment with noise

Figure 5-4: Samples from a part of the synthetic dataset, generated with the ray tracing: (a) clear (b) with additive normal noise.

Figure 5-5: Sample point cloud from the real part of the dataset. Tomatoes and a rubber ball are placed on a wooden support.

the Figure **??** the distribution of the algebraic distance from the ellipsoid surface is presented for the synthetic data. In the Figure **??** the same is given for the real data. It could be seen that the distribution for the real data is not unimodal and skewed for all three tomatoes considered, meaning that the real data does not fully comply with the used model.

The last considerable obstacle are the distortions that occur on the surface of the tomatoes. The exact reasons behind this effect are not clear, but such a distorted

appearance was noticed a number of times.

The ways to deal with these complications include the following. In order to account for the tomatoes being not precisely ellipsoid a more general model of the fruit can be used, such as hyperellipsoids or even the most general case, such as a combination of shperical harmonics. The noise with the complex distributions can be dealt with by standard RANCAS, as numerical experiments on the real data suggest. Finally, end-to-end algorithms, such as neural networks, can be used.

To test the algorithm on real data, a series of experiments was conducted with tomatoes located on a horizontal wooden board. The experiment involved six tomatoes and one rubber ball, that were placed at a distance of between 10 and 15 cm from each other, see Figure **??**. The camera captured scenes at various angles of the board: 55, 60, 70, 80 and 90 degrees. This made it possible to study the effect of the viewing angle on the perception of the shape of objects by the depth camera. For each angle, 146 point clouds were taken. Each point cloud contains approximately 111,000 points, where nearly 2,200 belong to the tomatoes. For a single object this number varies from 831 points for the nearest one to 130 for the farthest. The volume of the tomatoes ranges from 90 to 207 cubic cm. For each tomato the ball their actual size and volume were measured, and the exact location relative to the camera was determined. In this experiment, tomatoes were modeled as ideal spheres, where the radius of the sphere was determined by the average value of the semi-axes of the ellipsoid. The tomatoes used were reasonably close to a sphere, which made it possible to make this assumption fair. As a result, a dataset was created containing the centers and radii of objects, that were compared with the output of the algorithm.

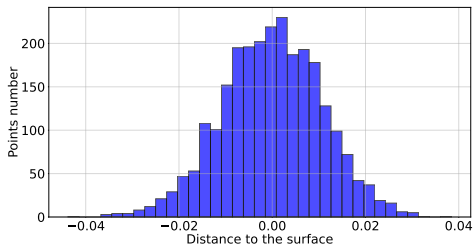

Figure 5-6: Distribution of the algebraic distance between the points and the surface of the best fitted ellipsoid model for synthetic data. A clear unimodal distribution can be seen.

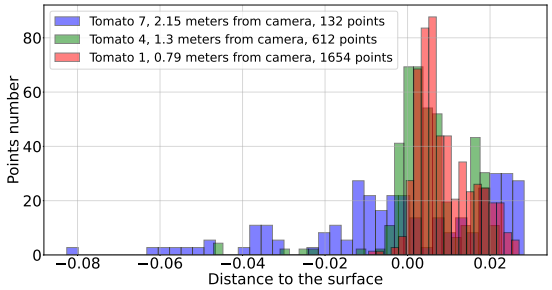

Figure 5-7: Distribution of the algebraic distance between the points and the surface of the best fitted ellipsoid model for three tomatoes from the real data. For all three of them the distribution is rather noisy and clearly not unimodal, suggesting that the real data is significantly more challenging than synthetic.

The real data was captured with Intel RealSense D435i. The exposure and white balance were set to auto. The scene was captured under artificial lighting.

Iterations	Full ellipsoids with noise				Ellipsoid segments with noise			
	0.0	0.01	0.26	0.41	0.0	0.01	0.03	0.05
10	1.0	0.9518	0.5428	0.5238	0.9978	0.2403	0.1582	0.1022
100	1.0	0.9523	0.5714	0.5569	0.9989	0.3079	0.1555	0.0969
1000	1.0	0.9427	0.5497	0.5219	0.9995	0.3885	0.2086	0.1333

Table 5.1: Average IoU with different number of iteration (10, 100 and 1000) on different data: full noised ellipsoids and noised ellipsoid segments, generated with ray tracing

Iterations	Full ellipsoids with noise				Ellipsoid segments with noise			
	0.0	0.01	0.26	0.31	0.0	0.01	0.03	0.05
10	0.0	0.0071	0.5214	0.7591	0.0008	0.2173	0.6498	0.6690
5000	0.0	0.0267	0.5527	0.1307	0.0	0.1394	1.7770	0.5463
10000	0.0	0.0091	0.0742	0.0336	0.0	0.1394	0.3276	0.4036

Table 5.2: Average Relative Volume Error with different number of iteration (10, 100 and 1000) on different data: full noised ellipsoids and noised ellipsoid segments, generated with ray tracing

5.5 Results

The experiments with the real data were conducted in accordance with the scheme in the Figure **??**: RANSAC for ellipsoids is applied after cutting a part of the point

Iteration number	**Precision**	**Recall**
1250	0.5346	0.8564
2500	0.5611	0.8445
5000	0.5697	0.8601
7500	0.5705	0.8623
10000	0.5798	0.8856

Table 5.3: Precision and Recall values for inliers for different number of iterations.

cloud that consists of the object only.

The metrics that were used to assess the method's performance are the following. First, it is the Intersection-over-Union between the real ellipsoid and the output of the algorithm. Second, it is the ratio between the predicted and real volume of the ellipsoid. Finally, it is the relative error in volume for the whole set of ellipsoids:

$$\frac{\sum V_{predicted} - \sum V_{real}}{\sum V_{real}}. \tag{22}$$

The hyperparameters used are the following:

- Threshold for the algebraic distance is 0.001
- Maximal iterations number is 10000. The results for the other iteration numbers are presented in the tables below
- Maximal acceptable ratio between the biggest and the smallest semiaxis is 2 (used for filtering)
- Maximal ratio between the maximal semiaxis of the ellipsoid and the maximal distance between the data points is 5 (used for filtering)

Figure **??** presents mutual distributions of a hypothesis IoU versus number of inliers for that model for different noise levels. For very strong noise, the constellation of dots in the plot appears as an almost vertical blob. It is bounded from the right, meaning that no model has lots of inliers. Consequently, the influence of the stochastic nature of the algorithm can lead to unsatisfactory results.

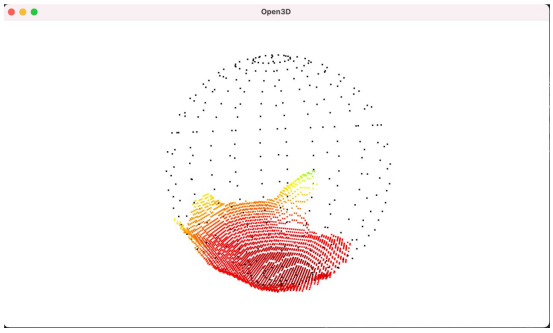

Figure 5-8: Output of RANSAC on a point cloud from the real data. Notice that despite the complexity of the data, i.e. small section of the ellipsoid covered, non-uniform density, surface distortion — the output is reasonably good. This exact sample was cherry picked for demonstration purposes.

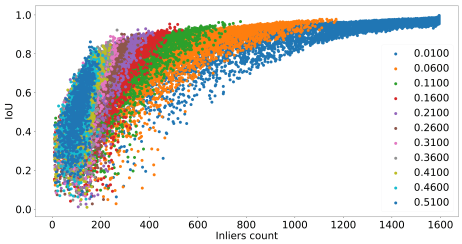

Figure 5-9: Mutual distribution of IoU and number of inliers for full ellipsoids with different noise amplitudes. A trend can be observed that generally the more inliers there are for the model, the higher the IoU with the true ellipsoid is.

On the other hand, with light noise a clear trend can be observed: with the growth of the number of inliers the quality in terms of IoU grows as well.

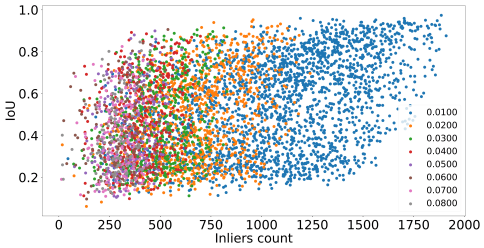

Figure 5-10: Mutual distribution of IoU and number of inliers for segments of ellipsoids with different noise amplitudes. In comparison with the Figure **??** the trend is much less prominent.

It could be noted that in the transition from the full ellipsoids to the segments, that are closer to the real data, the mutual distribution is blurred significantly, see Figure **??**.

Similar trend, but with the declining relative volume error can be observed on

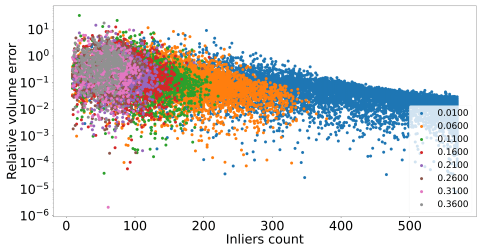

Figure 5-11: Mutual distribution of Relative Volume Error (RVE) and number of inliers for full ellipsoids with different noise amplitudes. With the growth of the number of inliers the average error declines.

the Figure **??**. For strong noise the number of inliers is small and the overall volume error is high, and for the light noise it is the exact opposite.

It could be observed that there it a noisy, but distinct trend of the increase in the model quality with the increase of the inlier number. However, due to the stochastic nature of the algorithm, it is not guaranteed that the best in terms of the IoU model will be the same that has the biggest inlier number.

Table **??** presents precision and recall for the inliers for the best fitted models. An improvement in the quality can be observed as the number of iterations grows. However, it is associated with a growing computtional burden, so a balance should be found for real applications between the quality of the output and the computational demands of the algorithm.

Now let us observe the dependence of the quality of the best model as the number of algorithm iterations increase.

The results for the different number of iterations are presented in the Table **??**.

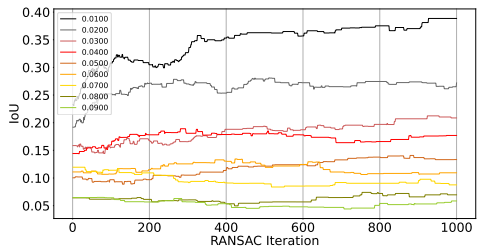

Figure 5-12: Dependency of IoU of the best model from the number of iterations for synthetic segments for different levels of noise. It is worth noting that overall with the growth of the iteration number there is a slight, but noticeable improvement in IoU.

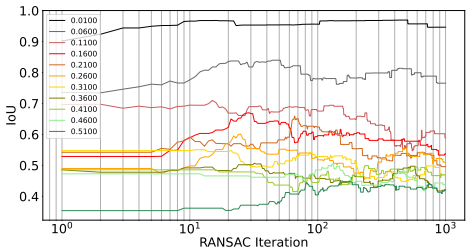

Figure 5-13: Dependency of IoU of the best model from the number of iterations for full synthetic ellipsoids for different levels of noise. x axis is logarithmic for better view. For light noise the IoU grows almost to 1.0 very rapidly (black line). For heavy noise the growth is much slower (green line).

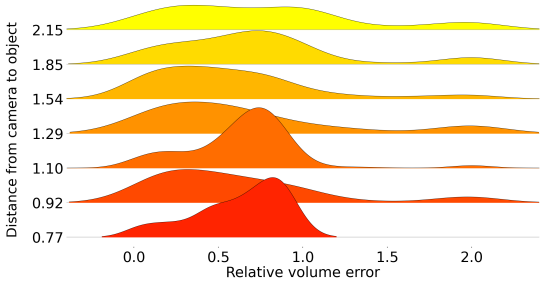

Figure 5-14: Distributions of Relative Volume Error for different distances from the camera for the point clouds filmed with 55 degrees between the camera direction and line of tomatoes

The best depth perception for Intel RealSense D435i is declared to belong to the range between 0.6 and 6 meters. However, Figure **??** as well as Figure **??** suggest that the variance in the distribution in the relative volume error grows significantly beyond approximately 1.5 meters. It can be explained by the decline in the infrared pattern density as the distance from the emitter increases.

The real applications are bounded by even more strict constraints in terms of the distance between the camera and the object. Since the distance between the rows of the tomatoes is limited by approximately 2 m, and the vegetation should be taken into account, the distance between the camera and the plant in the real environment is supposed to be from 0.5 to 1.5 m.

It could be seen from the Figure **??** that despite high variance in the relative volume error the average measured volume matches the real one very precisely. This result suggests that the method considered is applicable even under fairly noisy circumstances.

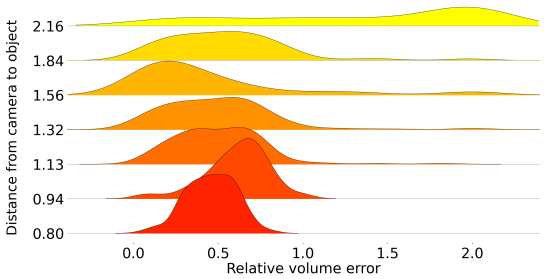

Figure 5-15: Distributions of Relative Volume Error for different distances from the camera for the point clouds filmed with 55 degrees between the camera direction and line of tomatoes

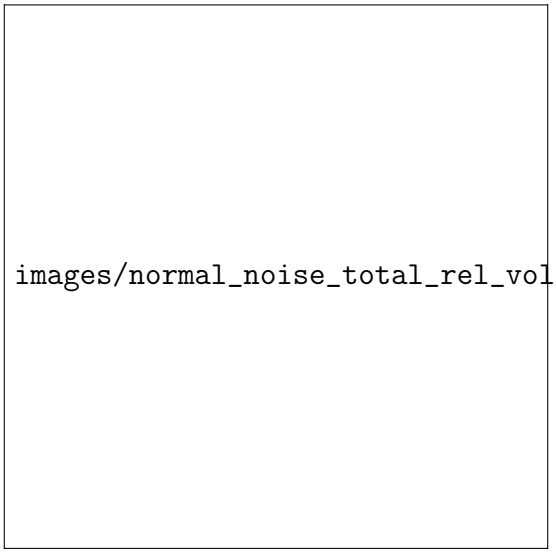

Figure 5-16: Dependency of the Total Relative Volume Error (sum over all the ellipsoids) on the number of iterations of RANSAC (logarithmic scale) for full noised synthetic ellipsoids. All the ellipsoids in the set have volume in the same order of magnitude. The noise level is 0.41.

Figure **??** presents the results of averaging the estimated volumes among all the point clouds for each tomato. The real volume is marked with a black dot. Despite high variance, the average volume is estimated with acceptable precision.

5.6 Conclusion

In this work an empirical study is carried out, aimed at examining the influence of noise on the performance of RANSAC method on quadric surfaces. A method for synthetic data generation with ray tracing was developed. The dependency of the error on the noise was examined on the synthetic point clouds. Experiments on the

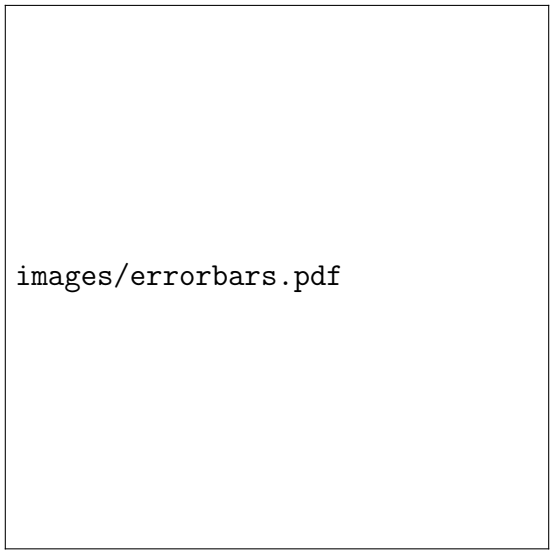

Figure 5-17: For each of the objects from the real dataset the volume was estimated for each of the point clouds. The average volumes with the error bars are listed along the axis represenating the distance from the camera to the object. The true volume for each of the tomatoes is marked with a thick black dot.

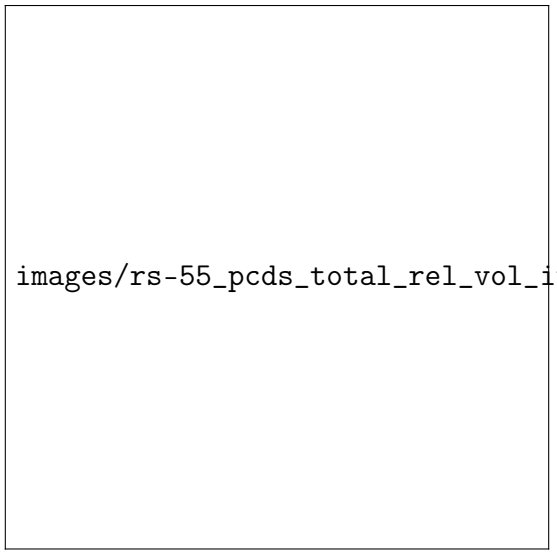

Figure 5-18: Dependency of the Total Relative Volume Error (sum over all the ellipsoids) on the number of iterations of RANSAC (logarithmic scale) for real data for different threshold values. The error clearly declines with the increase of the number of iterations.

real point clouds were carried out in the agricultural setting. RANSAC for quadric surfaces was implemented in Python.

As one may expect, the results suggest that noisy data is more challenging for the algorithm. The numerical evaluation of this phenomenon is given in the Results

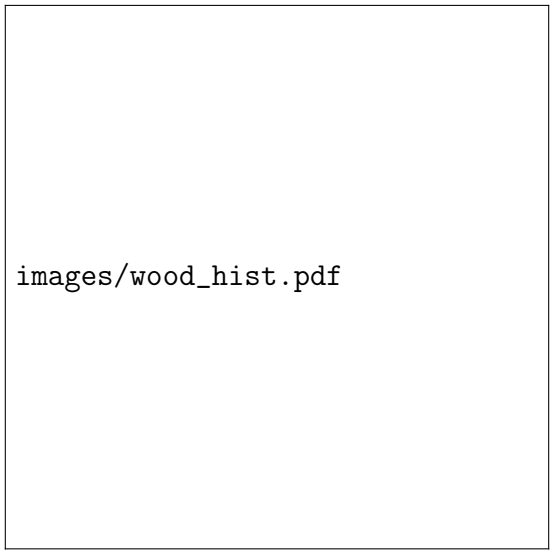

Figure 5-19: The distribution of the relative volume error for all the tomatoes from the dataset. The mean value is 1.0020. No additional scaling was applied.

section **??**. All in all, the qualitative findings are the following:

- The number of inliers for the model is correlated with its quality in terms of the output metric. This correlation becomes less prominent with the growth of the noise.
- On the challenging data the number of iterations plays crucial role in the quality improvement, see Figure **??** and **??** for results on synthetic data.
- IoU cannot be used as a single criteria for quality assessment, see Figure **??** and Figure **??** for a comparison of the plots for different noise levels.
- The quality of the output model declines with the growth of the distance from the sensor to the object. For the specific type of the camera that was used the cutoff distance that bounds the zone of reliable performance is nearly 1.5 meters.
- It was thus shown, that for the real data, which is the most challenging, RANSAC gives a high variance in the volume, but very small average error, which makes it applicable to the problem of yield estimation in the agricultural setting, see Figure **??**. The example of the algorithm's output is presented in the Figure **??**.

Ellipsoidal objects volume estimation by combining detection with RANSAC

I. S. Ryakin1,2, I. V. Osokin2, P. V. Osinenko2 1Moscow Institute of Physics and Technology 2Skolkovo Institute of Science and Technology

A method of ellipsoid volume estimation by noisy point cloud data is proposed. It relies on the combination of RGB and depth data. Specifically, it consists of two parts: detecting the objects in the RGB image, that is registered to the point cloud from a depth camera, and fitting ellipsoids to the corresponding subsets of that point cloud. The proposed method was tested on synthetic data and real data in agricultural context. Its main feature is that it is suitable for the real-world environments. For industrial applications, such as modern tomato greenhouses, it means that the tomatoes are not supposed to be manually picked. Volume estimation is a fundamental problem that has to be solved in a variety of real-world scenarios, ranging from agriculture[1,2] to medicine [3]. In contrast to many modern approaches, the proposed one does not rely on the contrastive background or an expensive setup with multispectral cameras. For the real experiments Intel RealSense D435i camera was used. The method's performance was evaluated on both synthetic and real data in terms of the Intersection over Union (IoU) between the predicted ellipsoid and the real one, volume error and processing time. The dependence of the output quality on the parameters, such as number of RANSAC iterations and inlier threshold, is presented. The method is compared with three other modern algorithms, showing superior performance on the complex real-world data. It is lightweight enough to be used on an autonomous agricultural robot with a user-grade laptop on board. To our knowledge there are no works that combine NN-based detection with robust volume estimation.

Figure 1. Proposed algorithm. First, RGB and point cloud data are obtained with distinct, but registered sensors. Second, NN-based detection is performed and point clouds corresponding to individual objects are extracted. Finally, RANSAC algorithm is used to fir the proper ellipsoid models to them, consisting of repetitive subsampling and model evaluation.

The contributions of this paper are as follows. A dataset of point clouds with tomatoes was collected in the environment closely mimicking the real greenhouse.

The dataset was marked, meaning that the tomato models were hand-fitted to the point clouds. Synthetic data was generated. RANSAC for quadric surfaces was implemented in Python. A pipeline consisting of YOLO [4] detection with subsequent point cloud cropping and RANSAC inference was realized. Numerical experiments were conducted. A comparison with modern approaches to ellipsoid estimation was made. It was thus shown that good enough performance could be achieved with the means of an autonomous robot and relatively cheap camera setup. The data was recorded data using both RGB and Depth channels, synchronized via standard RealSense SDK methods. Each tomato was physically marked for identification during post-processing. The lighting conditions were consistent, as the room was equipped with a window that blocks infrared light, and the overcast weather prevented direct sunlight. The proposed method was compared with three modern approaches on both synthetic and real data from the agricultural context. The first one is [5]. In this work a Bayesian approach to ellipsoid fitting was taken, that generalizes well even to higher dimensions. This algorithm maximizes the probability of the output model given the data, thus being robust to noise and out-of-distribution points. The second one is the implementation of Matlab Ellipsoid Fit [6]. In this work the problem of ellipsoid obtainment is approached with Linear Least Squares (LLSQ), followed by bringing the ellipsoid to the form of a quadric surface. Finally, the proposed approach was compared with [7]. The authors noted that in a lot of RANSAC implementations either the geometrical or algebraic distance was used in order to evaluate the quality of the model. An alternative approach was proposed, relying on the combination of the axial and Sampson distance, which gave high robustness against outliers and competitive processing time. The results are presented in the Tables 2, 3, 4 and 5. First, let us observe the metrics for different number of iterations for the best threshold are presented in the Table 1.

Iterations IoU Volume Error 10 0.2125 0.5084 100 0.2145 0.3587 1000 0.2164 0.2459

Table 1. IoU and Volume Error for different number of RANSAC iterations on real data

Let us compare the performance of the proposed method with the other algo-

rithms, see Tables 2, 3, 4 and 5.

Clean Models Normal Noise IoU Volume Error Time IoU Volume Error Time Bayfit 0.0078 0.1164 1.5849 0.0104 2.88e+25 0.3709 CAS 1.0 0.0 0.0037 0.7202 0.164 0.0174 Matlab Ellipsoid Fit 1.0 0.0 0.0003 0.8024 0.0925 0.0003 RANSAC (ours) 1.0 0.0 0.0297 0.5101 1.17 0.0297 Table 2. The comparison of the algorithms on clean and noisy full ellipsoids

Segment Clean Models Segment Normal Noise IoU Volume Error Time IoU Volume Error Time Bayfit 0.0005 0.3985 1.1149 N/A N/A N/A CAS 0.9899 0.01 0.0027 0.2054 4.0796 0.0029 Matlab Ellipsoid Fit 0.8447 20.8465 0.0006 0.1387 0.426 0.0005 RANSAC (ours) 0.9697 0.0192 0.0287 0.1985 2.1242 0.0298 Table 3. The comparison of the algorithms on Segment Clean data and Segment Normal Noise. N/A means that the algorithm did not provide a result

Real Data IoU Volume Error Time Bayfit 0.0185 0.9629 0.0657 CAS 0.1501 18.3553 0.0037 Matlab Ellipsoid Fit 0.0003 7.1066 0.0010 RANSAC (ours) 0.2237 0.7617 0.0254

Table 4. Real Data Results and Iterations

Year Lang Clean Noisy Clean Segm Noisy Segm Real Data Bayfit 2024 Matlab Yes Yes Yes No Yes CAS 2022 Matlab Yes Yes Yes Yes Yes Matlab Ellipsoid Fit 2018 Matlab/Python Yes Yes Yes Yes Yes RANSAC (ours) 2024 Python Yes Yes Yes Yes Yes Table 5. Summary of the methods. Yes and No for different data types denote if the method is working with them or not

On some of the synthetic data the proposed method performs worse than the other methods, see Normal Noise IoU, where Matlab Ellipsoid Fit gives higher IoU. However, on the most challenging sort of data, which is the real ellipsoids, the proposed method shows superior performance in terms of both IoU and volume error. Moreover, it could be noted that the average volume for a group of tomatoes closely matches real values, despite high variance in individual outputs, see Figure 2.

Figure 2. Distribution of the predicted volume divided by the real volume for all the tomatoes in the real data. Despite the variance being considerable, the mean value is nearly 1.05, which means that the main metric that the potential user will

be interested in, which is the volume estimation precision, is high.

Overall, a method of ellipsoid volume estimation was developed and tested in the real environment. Synthetic data was generated with gradual increase in complexity. A real dataset of point clouds and corresponding RGB images was gathered and marked. The dependence of the quality of the method's output on the iterations number was evaluated in numerical experiments, showing minimal average relative volume estimation error of 0.25. The comparison of the method with three alternative approaches was made, showing superior performance on the real data both in terms of IoU and volume error. It was thus shown that the proposed method can be applied to the real-world ellipsoid volume estimation. References 1. Nakaguro Y. et al. Volumetric 3D Reconstruction and Parametric Shape Modeling from RGB-D Sequences //Image Analysis and Processing—ICIAP 2015: 18th International Conference, Genoa, Italy, September 7-11, 2015, Proceedings, Part I 18. – Springer International Publishing, 2015. – P. 500-516. 2. Chaivivatrakul S. et al.TOWARDS AUTOMATED CROP YIELD ESTIMATION. 3. Rodriguez E. et al. Prostate volume estimation using the ellipsoid formula consistently underestimates actual gland size //The Journal of urology. – 2008. – V. 179. – №. 2. – P. 501-503. 4. Redmon J. et al. You only look once: Unified, real-time object detection //Proceedings of the IEEE conference on computer vision and pattern recognition. – 2016. – P. 779-788. 5. Zhao M. et al. A Bayesian Approach Toward Robust Multidimensional Ellipsoid-Specific Fitting //IEEE Transactions on Pattern Analysis and Machine Intelligence. – 2024. 6. Yury. Ellipsoid fit // MATLAB Central File Exchange : [Electronic resource]. URL: https://www.mathworks.com/matlabcentral/fileexchange/24693-ellipsoid-fit (accessed: 02.03.2025). 7. Han M. et al. Robust ellipsoid fitting using combination of axial and Sampson distances //IEEE Transactions on Instrumentation and Measurement. – 2023. – V. 72. – P. 1-14.

This work is focused on the development of a method of tangerine volume estimation based on the point cloud data. While monocular vision-based methods are often easier to implement and deploy in real world both in terms of algorithms and the sensors required, depth data is necessary to obtain precise volume estimate. In this work tangerines are approximated by ellipsoids, that are fitted to the point

clouds in 3D. A dataset of real tangerines was collected and marked. For each tangerine the mass and volume were measured. RANdom SAmple Consensus (RANSAC) was used for the ellipsoid identification. A number of experiments were conducted with varying algorithm hyperparameters, including iteration number and the inlier threshold value. The output quality was assessed via comparing the prediction of the method with the real volume of the fruit. Experimental results suggest that the good enough performance could be achieved in real time with a portable computer.

5.7 Introduction

Modern farming is characterized by both scale and efficiency. It is necessary to estimate the volume of the yield in order to plan the logistics and assess the quality of the produced fruit and vegetables. A big part of the measuring process nowadays is performed by hand, which is inefficient and prone to error. Thus, vision-based methods gain traction. They mainly rely on RGB sensors, and in certain cases depth cameras. While RGB-only sensors are much cheaper, depth information about the scene allows for more precise volume estimation. One of the key factors in the vision-based volume estimation is the noise that is an inherent property of the sensor data in the real greenhouse facility. In order to accommodate for these noises, robust volume estimation techniques should be applied.

Tangerines are one of the most important fruit in the agricultural produce worldwide**?**. This fruit could be approximated as an ellipsoid. An ellipsoid is described by 9 parameters: three coordinates, three semi-axis, and orientation. In this work episode model was used for the tangerines and the results show that this approximation allows for precise enough volume estimation.

Volume is one of the most important physical attributes of the fruit yield in agricultural production. The approaches to the measurement of the volume include the following. First, it is the physical examination of the fruit and measuring the volume with the underwater submersion. The second approach includes measuring the physical dimensions of the fruit and using a geometrical model to obtain the volume. Finally, a number of contactless approaches were proposed in the literature

recently, mainly relying on monocular or stereoscopic vision.

Let us briefly cover the main advantages and disadvantages of these approaches. On the one hand, monocular setups are often cheaper than stereoscopic. On the other hand, the performance of the monocular vision is limited by the inability of such methods to perceive true depth in the scene. Stereoscopic approaches capture the true volume better, but their usage is complicated by the setups being more expensive, bulky and difficult to work with.

5.8 Literature Review

Volume estimation is required in a number of real-world applicatioins, being used for planning, logistics, and automation. There are works dedicated to the evaluation of the volume of both structured and unstructured objects. The first group includes regularly shaped objects, like spherical oranges and cylindrical cucumbers. The second encompasses all the other objects, like piles of material or fruit with irregular shape. Both classes of problems can be approached with monocular or stereoscopic/depth-based setup.

In the monocular case, the most common method relies on the dividing of the object into slices with evaluating their volume basing on the geometric features, and adding the obtained volumes. Such is the work **?**, where the volume of Thai apple ber is evaluated.

In the case or irregularly shaped objects, similar approach can be applied **?**. The volume of the sweet potato is evaluated with adding all the volumes of the slices of the same height.

Another family of approaches can be used with regularly shaped objects only, such as tomatoes, tangerines and alike. A model is chosen that corresponds well to the object, and its parameters are fitted to the observed data **?**.

While multiview setup is used, both approaches remain feasible, but fitting model parameters is prevalent.

In the series of papers **?**,**?**,**?** authors propose the combination of the aforementioned approaches by combining slicing with circular slice parameters estimation

from two cameras.

However, slicing approach has a number of drawbacks, one of the most significant of them being the loss of precision while working with sparse point clouds. An examplary case of the ladder is **?**. This work is devoted to the estimation of the volume of pile-like objects, like stored sand or grain. The proposed method relies on the sampling of a voxel grid in accordance with the input point cloud.

Finally, there is a group of shape estimation techniques that rely on Random Sample Consensus (RANSAC) **?**. The presented work belongs to this class of methods.

5.9 Proposed Method

Let us briefly recap the classical RANSAC algorithm, starting from the motivation behind its development. After that, the method of tangerine volume estimation that was used in this work is described.

Shape recognition problem can be approached in a number of ways, with the simplest ones being not robust to noise and more sophisticated ones being computationally heavy. The simplest approach is the Least Squares Method (LSM). It is simple and straightforward, producing the output model with a number of straightforward matrix operations. In this method a quadratic error function is differentiated with respect to the model parameters, resulting in a set of equations. They are solved for the values of the parameters that minimize the quadratic error. However, this method has a number of drawbacks. The most crucial one is that LSM lacks robustness to noise. While presented with a data with strong outliers, least squares method incorporates those outliers in the calculation of the optimal model parameters, significantly degrading the quality of the produced model. Thus, LSM cannot be used if significant noise is present.

The second method that is oftem used for pattern and shape recognition is Hough transform **?**. In contrast to the previously mentioned method, this approach relies on the explicitly considering the discretized parameter space for all the possible models. For lines on the plane the dimensionality of the parameter space is two,

for circles it is three, for ellipses it is five, which (being implemented in the vanilla straightforward way) is already demanding in terms of the memory requirements.

In the presented work the dimensionality of the objects under consideration is nine, and the data is noisy, making both LSM and Hough transform not applicable.

Random Sample Consensus (RANSAC) is an iterative method of fitting the model to the data. It is capable of producing quality results even in the presence of high out-of-distribution noise.

In contrast to the Hough transform, RANSAC relies on a relatively small pool of models, lifting the memory consumption burden. Moreover, RANSAC does not take into account all the input points, thus being capable of disregarding outliers. On each step a small subset of data is randomly chosen. After that, a single model is obtained. The size of this subset allows one to specify a single unique model for the object considered. After the model is obtained, a number of data points that are represented well by this model is calculated.

The exact metric for the quality of the fitting can vary. The most straightforward way of evaluating that is measuring the distance from this point to the model. However, it is not always possible to find an analytical expression for that distance, leading to the lengthy iterative evaluation process. There is an alternative, relying on the algebraic distance. Algebraic distance is the value of the polynomial, that describes the object under consideration, be it curve or surface. There are other approaches to the measurement of the distance from the point to the model, in particular, a mixture of the geometrical distance and the distance measured along the semiaxes of the ellipsoid, as proposed in the paper **?**.

Overall, random sample consensus is a standard way pf solving a number of computer vision problems, including perspective transform evaluation, 3D reconstruction**?**, and pose estimation.

Regarding the drawbacks of RANSAC, it is computationally demanding, especially for complex objects. Thus, a balance should be found between the quality of the output and the performance requirements.

To our knowledge, there are no works on the application of RANSAC to the tangerine volume estimation. This paper aims to address this research gap.

The contributions of this paper are as follows.

- A dataset of point clouds with tangerines was collected in the environment mimicking the conveyor belt.
- Dataset markup was performed, meaning the measurement of the volume of all the tangerines.
- Numerical experiments were conducted with a self-contained Python implementation of RANSAC for ellipsoids.
- The results of the experiments were evaluated in terms of the volume error.
- The hyperparameters giving the best performance were identified.

It was shown that good enough performance could be achieved with the means of a user-grade active stereo camera and a modern laptop.

5.10 Experimental Setup

5.10.1 Algorithm Description

The input of the method is a number of three-dimensional points. The output of the algorithm is the volume of the tangerine.

Before the algorithm is applied, the data is collected and processed. The full volume estimation pipeline is as follows.

- An RGB image and a point cloud are taken with an Intel RealSense D453i camera.
- The tangerines are detected and segmented on the RGB image by the means of the color-based filtering.
- For each of the tangerines a corresponding point cloud is cropped.
- The obtained points are fed into the ellipsoid recognition algorithm.
- The volume of the tangerine is evaluated using the semiaxes of the ellipsoid.

5.10.2 Data Collection

The data was collected as follows. Thirty tangerines were arranged on a flat table surface in three rows of ten, see Fig. **??**. They were numbered sequentially from 1 to 30, moving from left to right. An Intel RealSense D435i camera was mounted above the table to capture images from a top-down perspective. After the images were taken, each tangerine was measured along its axes, and its volume was determined. The resulting point clouds were segmented into separate tangerine point clouds and a plane (table surface) using color filtering.

The characteristics of the tangerines captured are as follows.

- Minimum tangerine volume: 41.5 cm^3
- Maximum tangerine volume: 121.1 cm^3
- Average tangerine volume: 76.3 cm^3
- Smallest point cloud: 184 points
- Largest point cloud: 352 points
- Average point cloud size: 270 points

In total, 8 different camera positions were considered with the number of tangerines in the scene varying from 8 to 30. 205 frames were recorded for each scene, including an RGB image, a depth image, and a point cloud.

5.11 Results

The experiment results are presented below. Since the main quality metric is precision of volume estimation, the average volume error was evaluated.

Fig. **??** presents the values of the total volume error that was measured for all the tangerines, meaning that the total volume was compared with the ground true total volume, depending on the number or RANSAC iterations. A number of thresholds was considered. If the threshold value is too small, the output quality degrades as the number is the iterations grow, since the algorithm converges to fitting noisy

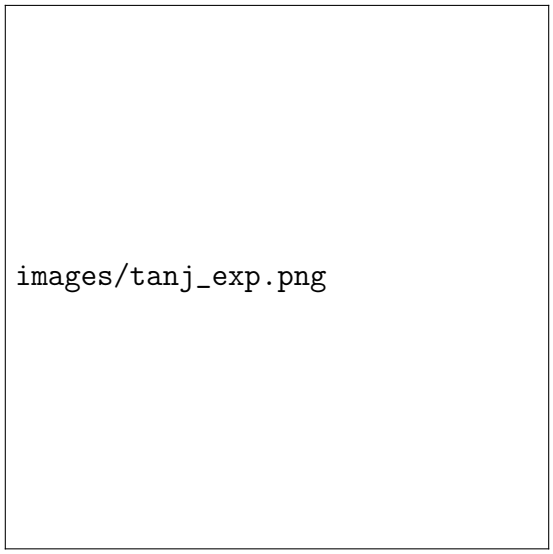

Figure 5-20: RGB frame from the dataset. It contains 30 tangerines. The images and the point clouds were captured by the means of an Intel RealSense D435i camera.

artifacts present in the data. With more reasonable threshold values the average volume error drops to nearly 0.1 over almost 200 iterations, making it possible to rapidly evaluate the volume of the tangerines.

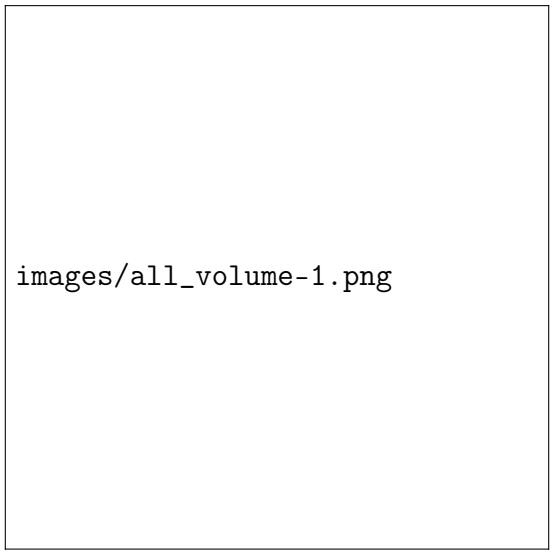

Figure 5-21: The dependence of the total volume error on the number of RANSAC algorithm iterations with different inlier threshold values. The best performance is achieved with the threshold values 0.001 and 0.00075.

Fig. **??** presents the values of the average volume error tangerine-wise, depending on the number or RANSAC iterations.

The numerical results across different iteration numbers and threshold values are

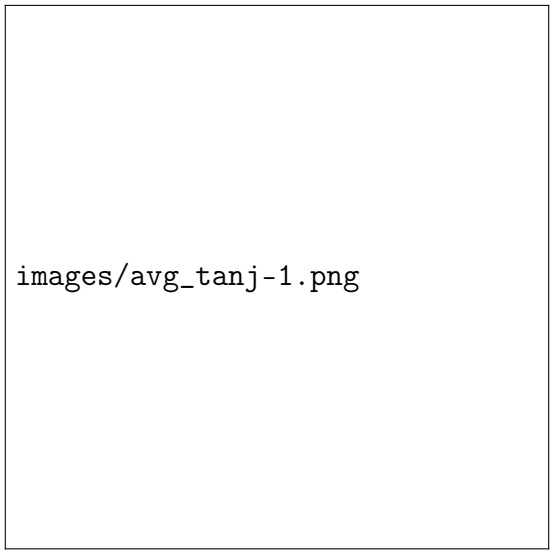

Figure 5-22: The dependence of the average volume error on the number of RANSAC algorithm iterations with different inlier threshold values.

presented in the tables **??** for total error and **??** for average error.

Table 5.4: Total Volume Error for Different Iterations Number across a Number of Thresholds.

Iterations	**Threshold**				
	0.0001	**0.0005**	**0.00025**	**0.00075**	**0.001**
10	0.3543	0.4482	0.5301	0.3227	0.4382
100	0.4136	0.2908	0.2942	0.2860	0.2968
1000	0.5078	0.2371	0.3265	0.2967	0.3328

Table 5.5: Average Volume Error for Different Iterations Number across a Number of Thresholds.

Iterations	**Threshold**				
	0.0001	**0.0005**	**0.00025**	**0.00075**	**0.001**
10	0.7013	0.8693	0.9357	0.6617	0.8053
100	0.4009	0.2301	0.3252	0.0939	0.1649
1000	0.5169	0.1644	0.3262	0.1688	0.1468

5.12 Conclusion

Overall, a method of robust volume estimation was applied to tangerines. A dataset of point clouds and RGB images was gathered, and the tangerines were measured

in terms of mass and volume. Numerical experiments were conducted with varying hyperparameters. The results suggest that Random Sample Consensus can be successfully applied in the problem of volume estimation.

The proposed approach has a number of applications in agriculture. First, it can be applied to the problem of the instant yield estimation. In order to assess the volume of the yield, a robot can be used that will monitor the agricultural facility and provide the estimated volume. Second, the measurements of the volume across different time periods can be helpful for the development of a prognostic tool for the prospective yield.

Future work can include the generalization of the method to other types of fruit, including non-elliptical ones. In particular, they can have a shape of a curved ellipsoid, like a banana, or a superellipsoid, like sweet pepper.

The proposed method can run on a normal computer with resonably computational load. In future RANCAS for ellipsoids can be adapted to the CUDA-based inference in order to speed up the computations.

Bibliography

J. Li, K. Lammers, X. Yin, X. Yin, L. He, J. Sheng, R. Lu, and Z. Li, "MetaFruit meets foundation models: Leveraging a comprehensive multi-fruit dataset for advancing agricultural foundation models," *Computers and Electronics in Agriculture*, vol. 231, p. 109908, 2025.

S. M. Mansuri, P. V. Gautam, D. Jain, N. C., *et al.*, "Computer vision model for estimating the mass and volume of freshly harvested Thai apple ber (*Ziziphus mauritiana L.*) and its variation with storage days," *Scientia Horticulturae*, vol. 305, p. 111436, 2022.

T. T. M. Huynh, L. TonThat, and S. V. T. Dao, "A vision-based method to estimate volume and mass of fruit/vegetable: Case study of sweet potato," *International Journal of Food Properties*, vol. 25, no. 1, pp. 717–732, 2022.

S. Jana, R. Parekh, and B. Sarkar, "A De novo approach for automatic volume and mass estimation of fruits and vegetables," *Optik*, vol. 200, p. 163443, 2020.

M. Khojastehnazhand, M. Omid, and A. Tabatabaeefar, "Determination of tangerine volume using image processing," *Tarım Makinaları Bilimi Dergisi*, vol. 4, no. 4, pp. 407–412, 2008.

M. Khojastehnazhand, M. Omid, and A. Tabatabaeefar, "Determination of tangerine volume using image processing methods," *International Journal of Food Properties*, vol. 13, no. 4, pp. 760–770, 2010.

M. Omid, M. Khojastehnazhand, and A. Tabatabaeefar, "Estimating volume and mass of citrus fruits by image processing technique," *Journal of Food Engineering*, vol. 100, no. 2, pp. 315–321, 2010.

Y. Ling, R. Zhao, Y. Shen, D. Li, J. Jin, and J. Liu, "DIVESPOT: Depth Integrated Volume Estimation of Pile of Things Based on Point Cloud," *arXiv preprint arXiv:2407.05415*, 2024.

M. Fischler and R. Bolles, "Random sample consensus: A paradigm for model fitting with applications to image analysis and automated cartography," *Commun. ACM*, 1981.

P. V. C. Hough, "Method and means for recognizing complex patterns," US Patent 3,069,654, Dec. 18, 1962.

M. Han, J. Kan, G. Yang, and X. Li, "Robust ellipsoid fitting using combination of axial and Sampson distances," *IEEE Trans. Instrum. Meas.*, 2023.

I. Nyalala, C. Okinda, L. Nyalala, N. Makange, Q. Chao, L. Chao, K. Yousaf, and K. Chen, "Tomato volume and mass estimation using computer vision and machine learning algorithms: Cherry tomato model," *Journal of Food Engineering*, 2019. Yield volume estimation is the integral part of modern farming. While classical model-based approaches are already well-developed, in the recent years neural network-based end-to-end methods gain traction. This work is devoted to the case study of applying a PointNet++-like neural network to the problem of tangerine volume estimation with the point cloud data. A set of tangerines filmed by Intel RealSense camera was collected and marked. The dataset includes RGB images and depth images. The volume estimation method is run on this data presented in the form of point clouds. A number of experiments on this dataset were conducted. Experimental results suggest that the problem of volume estimation on the real data can be solved by the means of a single modern computer in real time. The output quality was assessed via comparing the prediction of the method with the real volume of the fruit. The average volume estimation error slightly exceeds 10%.

5.13 Introduction

In modern farming it is necessary to estimate the characteristics of the yield in order to plan the logistics properly and assess the quality of the product. Volume is a key physical attribute of the fruit yield in agricultural production, and tangerines are one of the most important fruit in the agricultural produce worldwide**?**. An ellipsoidal model can be used to approximate this fruit with 9 parameters: three coordinates, three semi-axis, and orientation. The physical examination of the fruit and measuring the volume with the underwater submersion can be used, as well as the measurement of the physical dimensions of the fruit and using a geometrical model to obtain the volume. However, this approach is excessively labour-intensive and requires manual manipulation of the fruit. Thus, a number of contactless approaches were proposed, mainly relying on monocular or stereoscopic vision.

5.14 Literature Review

Shape and pattern recognition were developed since the dawn of the modern computers. The first methods like Hough transform **?** were applied in 1960s to the problem of recognizing tracks in the bubble chamber to analyze the behavior of the particles in the accelerator. The automation of the recognition significantly reduced the burden of data processing for scientists and engineers, making it possible for them to focus more on the substance of their experiments instead of tedious measurements and calculations performed by hand. A number of robust methods were developed, capable of extracting the meaningful information from the noisy data. Suddenly it has become possible to analyze large quantities of data in short time by the means of computers.

Several decades later shape and pattern recognition methods started to be applied in other areas of human activity. In particular, they are nowadays used in document recognition, medicine, monitoring, and security. Regarding the agricultural applications, pattern and shape recognition has a variety of applications. They in-

clude activity monitoring of human workers, safety monitoring, disease detection, crop loss prevention and yield estimation.

In order for the supply chain to function properly it is necessary to estimate the yield that can be harvested at a certain facility. This includes the number of fruit and their total mass, which is often simply proportional to the volume. If the yield estimation is performed by human workers, it could be slow and prone to error. Moreover, manual assessment is a boring and tedious task, requiring facility inspection during prolonged periods of time. Automated methods of yield estimation are already introduced into the market, but they are not adopted everywhere yet.

Among all the methods of automated monitoring of the agricultural facilities, computer vision-based methods are applied more frequently than the other. It can be attributed to the advantages of the vision channel of perception. Computer vision-based methods allow for contactless monitoring. Digital cameras are already well-developed and cheap enough for them to be widely adopted. Moreover, there already exists a wide range of methods that could be straightforwardly applied to the problems of classification, detection, segmentation and regression in the agricultural context.

Some of these problems are more straightforward to solve than the other. In particular, the development of a system to detect the object in the greenhouse is streamlined to the collection of the dataset and training and already existing model of YOLO family **?**, which often gives a solution as good as the data allows. The classification problem can be solved in the similar manner, considering a case of RGB monocular images. Overall, monocular image processing in agricultural context could be considered to be in almost solved problem. There are a number of works with the classical computer vision approaches being applied to volume estimation, see **?**, **?**.

When it comes to the stereoscopic setups or point cloud processing, the number of widely available tools becomes smaller. There are two major families of approaches in this field. First of them relies on the classical shape recognition techniques like least squares, Hough transform or Random Sample Consensus (RANSAC)

?. While the first approach is sensitive to the noise, and the second is heavy on memory consumption, RANSAC is capable of solving the problem of fitting complex objects with a lot of parameters, such as ellipsoids.

Let us briefly recap the widely adopted approach to the volume estimation with this method, applied to the ellipsoid-like objects like tomatoes and tangerines. First, the point cloud data is obtained by a camera that is aligned with an RGB sensor. After that, all the objects of interest are detected. The point clouds that correspond to this object are extracted. Finally, RANSAC is applied to fit a single model to the object. This method allows one to estimate the volume, since the model includes three semiaxes of the object, and if it could be approximated as an episode, the volume of the fitted model will be close to the volume of the object of interest.

RANSAC relies on multiple samplings of a small subset of the input data. For each subset, a single model is fitted. After that, it is measured against all the input data points and it is evaluated how good or bad does this model describe the entirety of the input. The output of the method is the model that corresponds the best to the input points, excluding the out-of-the-distribution noise, which is inevitable in real data in a greenhouse facility. This method is widely used and developed, still receiving attention from the community, and it is modified in certain details, such as the method of measuring the distance from the model to the point **?**.

With all the advantages of this method, there are a number of drawbacks. Due to the iterative manner of model generation, RANSAC can require significant computational power. Constructing the model of a high-dimensional object is heavy on computations as well. The development of a method to obtain a model from a set of points requires manual engineering for each new type of objects under consideration. Moreover, RANSAC relies on a number of assumptions and hyperparameters that should be manually tuned.

It could be noted that in order to evaluate the volume of the object it is not necessary to construct its full model. A representation of the object should be constructed, but it is not required to include the coordinates and the orientation. Recent advancements in neural networks make it possible to develop an end-to-end

method of volume estimation, bypassing the construction of the full model.

The nature of point cloud data requires a specific approach for it to be processed by a neural network. While some of the most widely used types of neuron networks, like fully-connected or convolutional, are capable of approximating complex functions, learning dependencies, and producing state-of-the-art results in a number of applications, they cannot be directly applied to the raw point cloud data. Point clouds are sets of three-dimensional points, in certain cases with color. The model that will process this data should ideally be invariant to the permutations in the data. It was shown to be difficult to enforce such a property to a standard neural network. They could be applied to the data if the point cloud is transformed with the methods like voxelization, but this approach leads to significant growth of the computational complexity. Point clouds are inherently sparse, and this property should be taken into account while the method is developed.

In 2016 a novel approach PointNet **?** was proposed. It relies on the processing of all the data points individually and then extracting the necessary features from the point cloud of variable size, which is not possible with the other, standard approaches. Another novelty of PointNet is the application of two smaller networks, that are used to generate rotation matrices that are transforming the data before it is fed into the main network. Further advancements in the development of the PointNet family include joining them with the generalization of convolution **?**, that was developed specifically to fit the demands of the point cloud data. With these generalized convolutions the local features of the point cloud could be taken into account, which is beneficial for the end result.

In this work a PointNet++-like model was used.

The contributions of this paper are as follows.

- A dataset of point clouds with tangerines was collected in the environment mimicking the conveyor belt.
- Dataset markup was performed, meaning the measurement of the volume of all the tangerines.
- Numerical experiments were conducted with a PointNet++-like neural net-

work on ellipsoids.

- The results of the experiments were evaluated in terms of the volume error.

Fig. **??** presents a point cloud from the dataset, captured by Intel RealSense D435i.

5.15 Experimental Setup

5.15.1 Algorithm Description

The input of the method is a number of three-dimensional points. The output of the algorithm is the volume of the tangerine. Before the algorithm is applied, the data is collected and processed. The full volume estimation pipeline is as follows.

- An RGB image and a point cloud are taken with an Intel RealSense D453i camera.
- The tangerines are detected and segmented on the RGB image with the color-based filtering.
- For each of the tangerines a corresponding point cloud is cropped.
- The obtained points are fed into the neural network.

5.15.2 Data Collection

The data was collected as follows. Thirty tangerines were arranged on a flat table surface in three rows of ten. They were numbered sequentially from 1 to 30, moving from left to right. An Intel RealSense D435i camera was mounted above the table to capture images from a top-down perspective. After the images were taken, each tangerine was measured along its axes, and its volume was determined. The resulting point clouds were segmented into separate tangerine point clouds and a plane (table surface) using color-based filtering.
The characteristics of the tangerines captured are as follows.

- Minimum tangerine volume: 41.5 cm^3

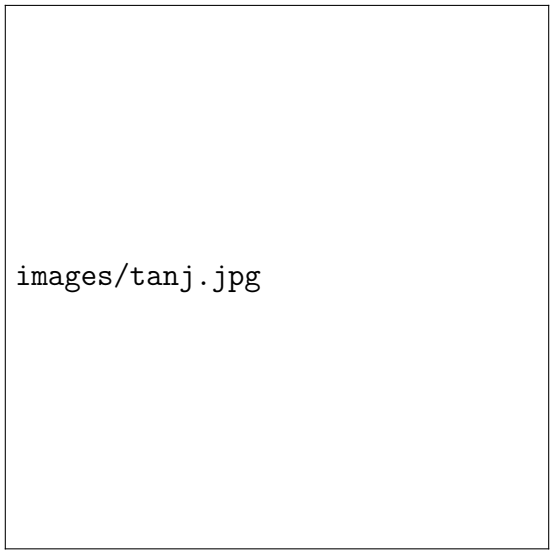

Figure 5-23: An example of a point from the dataset, containing 30 tangerines. The images and the point clouds were captured with Intel RealSense D435i camera.

- Maximum tangerine volume: 121.1 cm^3
- Average tangerine volume: 76.3 cm^3
- Smallest point cloud: 184 points
- Largest point cloud: 352 points
- Average point cloud size: 270 points

In total, 8 different camera positions were considered with the number of tangerines in the scene varying from 8 to 30. 205 frames were recorded for each scene, including an RGB image, a depth image, and a point cloud.

5.15.3 Neural Network Architecture and Training

The neural network encompasses 393025 parameters. All the point clouds in the dataset containing 30 tangerines were split into 7980 for training and 3990 for test.

Fig. **??** presents the architecture of the neural network, closely following PointNet++ **?**. It consists of the following parts. First, a number of spatial processing sections are appiled. The spatial processing section is a crucial part of this architecture. It subsamples a number of points from the neighborhood of each point, conserving local distibution of the points. After that, the points are grouped and

a vector representation for them is obtained via multilayer perceptron, followed by max pooling. After three spatial processing sections global max pooling is performed. Finally, a series of fully connected layers are used.

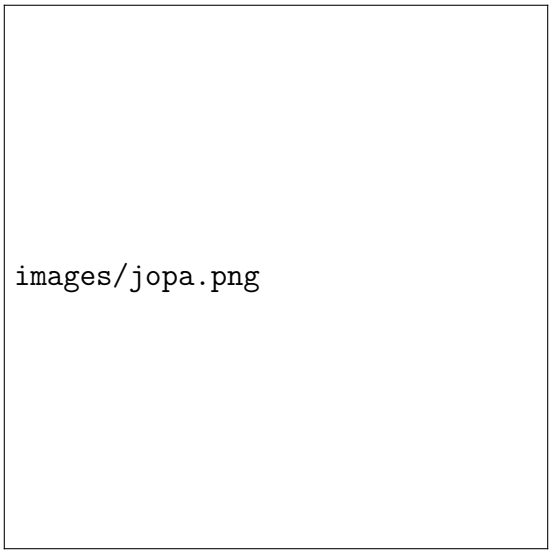

Figure 5-24: The architecture of the neural network used in the work.

5.16 Results

The training took 89.5 minutes on a computer with processor Intel Core i5-13400 (13th Gen, 10C/16T, 2.5 GHz), 32 Gb of RAM DDR5 and graphics card NVIDIA GeForce RTX 4070 (12 GB GDDR6X). The inference time on a single point cloud is 290 milliseconds.

The results are presented below. Since the main quality metric is precision of volume estimation, the average volume error was evaluated.

Fig **??** presents the values of the loss function as the training progresses. It could be noted that after epoch 30 the decline stagnated, meaning that the generalization capabilities of the model and the quality of the data do not allow for the further improvements. Fig. **??** presents the dependence of the average volume of the number of epochs of training.

The main result of the presented work is the following. After the training the Mean Relative Volume Error on the real point cloud data with tangerines from the test set reached 0.1070. Overall, the performance meets the demands of the market in

Figure 5-25: The dependence of the loss function on the training epoch.

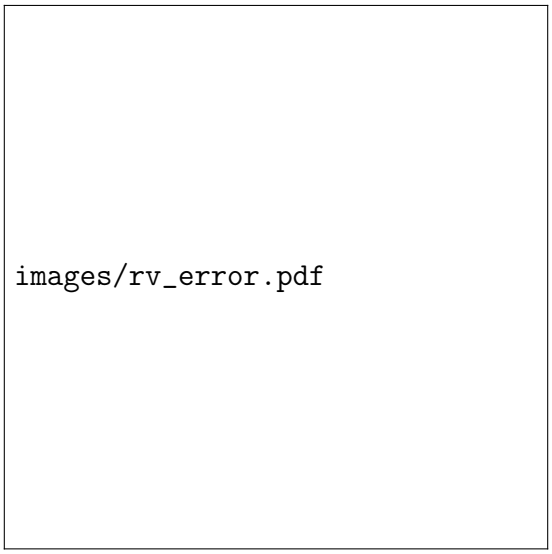

Figure 5-26: The dependence of the Relative Volume Error on the epoch.

terms of the quality of volume estimation and inference time on a modern laptop. The sensor used is a user-grade active stereo camera.

5.17 Conclusion

Overall, a neural network-based end-to-end tangerine volume estimation method was proposed. It relies on the PointNet++ architecture. The training on the custom dataset takes nearly 1.5 hours, and the error in the volume estimation lightly exseeds 10%.

The inference time of 290 milliseconds allows for the real-time onboard inference with limited computational resources. The proposed approach can be used on mobile robots for the agricultural facilities monitoring.

Bibliography

J. Li, K. Lammers, X. Yin, X. Yin, L. He, J. Sheng, R. Lu, and Z. Li, "MetaFruit meets foundation models: Leveraging a comprehensive multi-fruit dataset for advancing agricultural foundation models," *Computers and Electronics in Agriculture*, vol. 231, p. 109908, 2025.

P. V. C. Hough, "Method and means for recognizing complex patterns," US Patent 3,069,654, Dec. 18, 1962.

J. Redmon, S. Divvala, R. Girshick, and A. Farhadi, "You only look once: Unified, real-time object detection," in *Proceedings of the IEEE Conference on Computer Vision and Pattern Recognition*, pp. 779–788, 2016.

I. Nyalala, C. Okinda, L. Nyalala, N. Makange, Q. Chao, L. Chao, K. Yousaf, and K. Chen, "Tomato volume and mass estimation using computer vision and machine learning algorithms: Cherry tomato model," *Journal of Food Engineering*, 2019.

M. Ghahremani, K. Williams, F. Corke, B. Tiddeman, Y. Liu, X. Wang, and J. H. Doonan, "Direct and accurate feature extraction from 3D point clouds of plants using RANSAC," *Computers and Electronics in Agriculture*, vol. 187, p. 106240, Aug. 2021.

M. Fischler and R. Bolles, "Random sample consensus: A paradigm for model fitting with applications to image analysis and automated cartography," *Commun. ACM*, 1981.

M. Han, J. Kan, G. Yang, and X. Li, "Robust ellipsoid fitting using combination of axial and Sampson distances," *IEEE Trans. Instrum. Meas.*, 2023.

C. R. Qi, H. Su, K. Mo, and L. J. Guibas, "PointNet: Deep learning on point sets for 3D classification and segmentation," in *Proceedings of the IEEE Conference on Computer Vision and Pattern Recognition*, pp. 652–660, 2017.

H. Thomas, C. R. Qi, J.-E. Deschaud, B. Marcotegui, F. Goulette, and L. J. Guibas, "KPConv: Flexible and deformable convolution for point clouds," in *Proceedings of the IEEE/CVF International Conference on Computer Vision*, pp. 6411–6420, 2019.

C. R. Qi, L. Yi, H. Su, and L. J. Guibas, "PointNet++: Deep hierarchical feature learning on point sets in a metric space," *Advances in Neural Information Processing Systems*, vol. 30, 2017.

Chapter 6

Disease detection

Let me introduce to the topic of my PhD work at Skolkovo Institute of Science and Technology (SK).

6.1 Thesis Structure

The diagram in **??** illustrates the flow of information through the structure of the thesis.

?? - Background Here's the literature review.

?? - Thesis Objectives We define the objectives of our work.

...

?? - Conclusion In the last chapter, we discuss our results obtained ...

Modern agriculture poses several challenges in terms of the requirements for monitoring speed and precision. Certain greenhouses of the major agricultural companies are so huge, that it is virtually impossible to timely examine the whole facility with a reasonable human workforce. While it is possible to introduce more and more human workers, a sustainable long-term solution is to use autonomous robots to automate such repetitive tasks.

While robot-assisted agriculture has been developing for a long time already, the integration of a robot into an industrial-scale production often demands

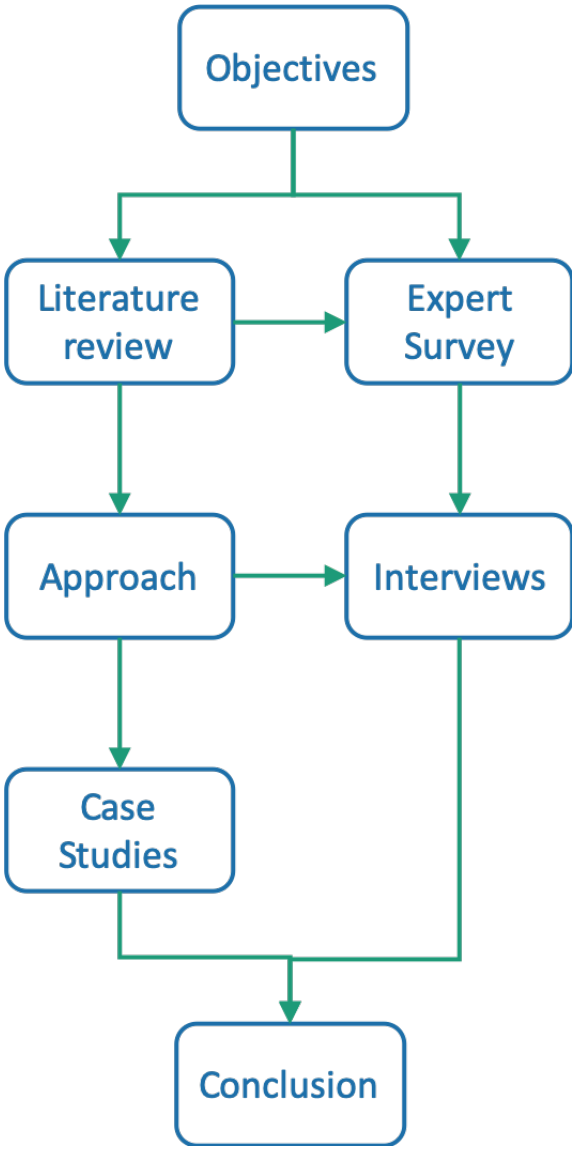

Figure 6-1: Thesis structure

substantial effort. It requires the robot to have a high degree of autonomy while keeping the modifications that the greenhouse facility should go through to the minimum.

6.1.1 Target environment

The target greenhouses for this project are rectangular 120000 m^2 (12 hectares) buildings with glass rooftops. During the night and in cloudy weather red-blue LEDs are used to provide sufficient lighting. The temperature and humidity

are kept stable at all times. Several types of tomatoes are grown there with the help of hydroponics. One tomato plant grows up to 35 meters in length during 10 months of cultivation. The majority of the length of the plant is kept horizontal, and the top of the plant is at a height of approximately 4 meters.

6.1.2 Powdery mildew

The density of the biomass (see Figure **??**) in these greenhouses allows for cost savings because of the scale of the production. On the other hand, it leads to the rapid spread of various kinds of bacterial infections, fungi, viruses, and insects. Thus, timely monitoring in such greenhouses is crucial. Powdery mildew is known to infect the lower leaves first and then spread up the plant. It develops best at temperatures slightly below 30°C and high humidity, which are precisely the conditions that the tomatoes are grown in for the great portion of the production cycle. Thus, the development of the powdery mildew is rapid, taking 4 to 7 days to progress from early to medium stage **?**.

Figure 6-2: Image taken in a greenhouse at the top of the plants.

With the aforementioned requirements for monitoring speed in mind, an autonomous robot on an omnidirectional platform was developed and manufactured. It is equipped with cameras, covering the whole height of the tomato

plant, and an onboard computer to process the data in real-time.

This paper presents a work on the data acquisition with this robot, as well as coordinating the markup procedure by human experts and a comparison of the performance of several neural networks.

6.1.3 Datasets available and related work

The majority of the open datasets are either small or taken in laboratory conditions, meaning professional cameras, artificial lighting, separation of the leaves from the plant, or manual preprocessing. By far the most popular dataset in the field **?** consists of images of leaves on a contrastive background. Collecting such a dataset is expensive, and its usage is limited by the differences between the laboratory and real conditions.

While there are several publicly available datasets out there, relying on them could be risky due to the covariance shift **?**. The main difficulties for obtaining qualitative and consistent markup are**?**:

- Symptom variations.
- The potential presence of different disorders with similar symptoms.
- Ill-defined edge cases, leading to the markup ambiguity.

Taking into account all the aforementioned factors, a dataset for classification, consisting of images from the target greenhouse in normal conditions was collected and marked, see section **??**. It is worth noting that accuracy is by far the most used evaluation metric in the field of automatic plant disease detection **?**.

6.1.4 Related work

There are multiple solutions to the same problem that were stated in different environments. They can rely on hyperspectral imaging **?**, **?**, **?**, **?**, on recurrent NNs **?**, a custom convolutional architecture **?**. Hyperspectral cameras are

usually expensive, which limits their availability. In this work, relatively cheap user-grade RGB cameras were used.

There are several works that are aimed at comparing the performance of already widely adopted models on specific tasks, such as **?**, **?**, and **?**. The aim of this work is to produce a solution that fits the specific needs of the environment from an engineering standpoint, see section **??**.

6.1.5 Contribution

The contributions of this paper are as follows:

- Roboticised data acquisition was performed. Namely, a robot was designed and manufactured, and a dataset of powdery mildew-infected tomato leaves was gathered. The data collection was performed in a real environment under varying lighting conditions.
- Marking of the 6817 images into positive and negative classes was coordinated. The markup was performed by human experts with formal education in agriculture. The consistency of the experts was assessed by providing the same samples to different experts.
- Using this data, an experiment was conducted: YOLOv8 (n, s, m), EfficientNet (V2l, B3, B4), ResNet (34 and 152), MobileNetV3 (small and large) were compared in terms of their accuracy and the inference time on the target computer.
- It was thus demonstrated that good enough performance could be achieved with the means of user-grade cameras and images that were taken from the moving robot. The mutual expert consistencies were matched by the NN model in terms of the classification accuracy, see section **??**.

The paper is structured as follows. First, the mechanical platform is briefly described and an overview of the solution to the disease detection problem is given. Second, the data acquisition and markup procedures are described. Third, the training in terms of the models, parameters, and experiments is

described. Finally, a comparison of the performance of different NN models is given.

6.2 Platform

With a prospective weight of the robot of around 100 kilograms, an aluminum frame made of a profile with a square cross-section was designed. The design of the chassis was performed with the intent to minimize the number of individually actuated elements. The result is an omnidirectional platform with 4 identical wheel pairs.

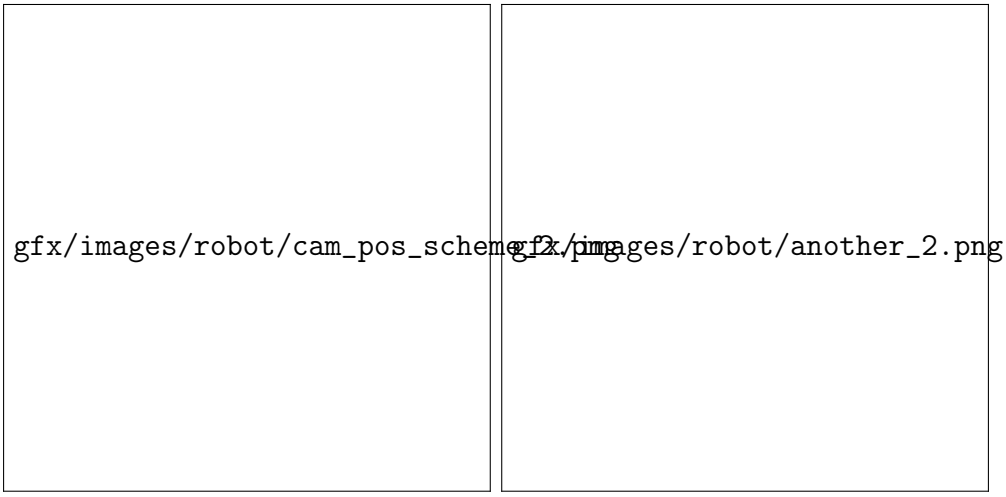

(a) (b)

Figure 6-3: (a) Sketched Fields of View of the cameras. (b) Physical assembly during the data acquisition.

The power supply and consumption of the robot could be summarized as follows:

- 6 × 24 Ah 48 V LiNCA batteries
- 144 Ah (approximately 7 kWh)
- Nearly 14 hours of uptime on one charge with the power consumption of 500 W

One of the crucial decisions that had to be made was the positioning of the host computer for the NNs inference. The final design of the robot included a

relatively powerful computer on board, see section **??**. It would be reasonable to do this in another way – by dividing the system into a robot and an external server. This would bring the problem of providing coverage of the entire greenhouse with a wireless network capable of broadcasting a number of (at least) FullHD videos in real-time.

6.3 Overview of the solution

For the problem of tomato greenhouse monitoring the main requirements for the vision system are the following.

First, the combination of the Fields of View (FoV) of the cameras should cover the entire height of the plants, from the tomatoes to the tips of the vegetation. Diseases, parasites, and damage can occur anywhere on the plant. This requirement is addressed by installing a number of cameras, their proper positioning, and their parameters. Three web cameras were utilized. The sketch of this setup is given in Figure **??**, and the real assembly is given in Figure **??**. At this point, only one side is covered by combined FoVs, but it is planned to replicate that and cover the other side as well.

Second, the image processing should be performed in real-time. Ideally, the robot is expected to spend all the time in the field moving. With real-time processing, it is possible for the workers to rapidly examine specific rows of tomato plants. The robot should be capable of observing the same part of the plant from different locations, meaning that the data processing should happen in real-time with a certain overlap in the frames.

During the design of the vision subsystem, the following assumptions were adopted. In the initial testing, the robot was moving at a speed of 0.26 m/s, which is a safe value for indoor applications. Considering potential acceleration for the sake of faster monitoring, an upper-speed limit could be set to 0.5 m/s. The horizontal FoV for the chosen optics covers 1.07 m. Thus, moving an object through it from left to right takes nearly 2 s. To assure the 5-fold

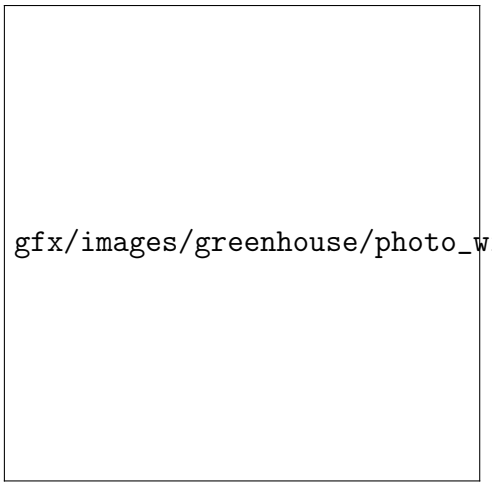

(a) Image of powdery mildew-infected leaves.

(b) A scattering of white patches is a clear visual sign of the presence of the disease.

Figure 6-4: (a) Image from the bottom camera of the robot. (b) Zoomed in.

overlap, each of the cameras has to capture an image at least once every 0.4 s. That results in the requirement for the processing speed of 8 frames of 1056 $\times$ 1056 pixels per second. This requirement is met with a huge margin.

6.4 Data markup and quality evaluation

A set of approximately 300000 images was collected with some of them exhibiting manifestations of the powdery mildew, see Figures **??**, **??**. In order to obtain a dataset of a reasonable size, every 30-th frame was chosen, resulting in approximately 10000 frames that are uniformly distributed across the entire original dataset.

The process of the data labeling was organized as follows. At each of the 4 iterations, each of the experts was provided with 550 images of the tomato leaves, which had to be separated into two classes: negative and positive. Among these 550 images, there were 500 unique for each expert and 50 images shared by all the experts in order to assess their consistency. The mutual consistencies of the experts in the subsets are given in Table **??**.

It is worth noting, that the major part of inconsistencies occur as a conse-

quence of the frame quality. It is possible to overcome this issue by reducing motion blur with the help of the cameras with a global shutter, however, this work shows that the target problem can be solved with cameras with a rolling shutter.

6.5 Training

6.5.1 Hardware

A two-tier computing strategy for training and testing the neural networks was used. The training was performed on a stationary server: Intel Core i9-9900 3.10 GHz, GeForce RTX 3080, 32 Gb. Testing was carried out on the target device - the robot's onboard computer. Its performance is much more limited: Intel Core i5-11400H 2.70 GHz, GeForce RTX 3050Ti laptop, 16 Gb. Both machines operated under Ubuntu 20.04.

6.5.2 Models

A comparison of 10 top-performing classification models provided by Roboflow **?** was carried out. These models encompass:

1. Three versions of YOLOv8**?**: YOLOv8n, YOLOv8s, and YOLOv8m.
2. Three versions of EfficientNet**?**: EfficientNetV2l, EfficientNetB3 and EfficientNetB4.
3. Two versions of ResNet**?**: ResNet34 and ResNet152.
4. Two versions of MobileNet**?**: MobileNetV3small and MobileNetV3large.

6.5.3 Data sampling

Three distinct datasets were created, each addressing the class imbalance challenge within the original dataset. Initially, the data comprised 5684 instances

of the negative class and 1133 instances of the positive class. To tackle the imbalance, three different strategies were pursued:

- For the first set 1133 images of the negative class were randomly selected, equalizing the number of photos in both classes.
- For the second set all the photos from the positive class were duplicated to increase the number of original images of the negative class. The number of training photos per class grew from 850 to 1700.
- For the third set, all the labeled data available was used. To achieve this, extensive and diverse augmentation techniques were applied. The positive class images were duplicated six times with augmentation, and similar augmentation transforms were applied to $\frac{6}{7}$ of the negative class images. This training set consists of 5361 instances of the positive class and 5316 instances of the negative class.

In all the experiments 75-15-10 % train-val-test split was used.

6.5.4 Data Preprocessing

Resizing: All the images underwent cropping to a square shape and a resizing process with the resultant dimensions of 1056 $\times$ 1056 pixels. The rationale behind adopting this specific size is the following. First, some of NN models that were planned to be used could work only with the image sizes that are multiples of 32. Second, the downscaling of the images was not feasible, because powdery mildew appears with quite small features, and reducing the image size would entail a substantial loss of critical information. Third, resizing rectangular images into a square will again lead to the loss of data.

Augmentation: Across all three datasets, a standardized suite of transformations was applied. These transformations encompassed horizontal and vertical flipping, shifting, rotation, and HSV color transformation. However, it is worth noting that the third dataset underwent a more expansive augmentation strategy. For this subset, the following augmentations were applied:

- *Predominantly:* Defocus, stochastic mist, noise injection, RandomBrightnessContrast, and HSV color transformation featuring augmented values.
- *To a smaller extent:* ColorJitter, rgbshift, ChannelShuffle, ChannelDropout, image inversion, and sepia.

The selection of these augmentation techniques aimed to diversify the dataset as much as possible to enhance the model's generalization capabilities.

6.5.5 Experimental setup

The setup in terms of the training is the following:

- Training the majority of the models for 40 epochs before choosing the best checkpoint. The exact number for each model is given in the table ??.
- SGD optimizer was used.
- The default values for the learning rate of 0.01 for YOLO models and 0.001 for other models were used.

The choice on the number of epochs was made following preliminary training runs with the learning curves stagnating after such a number of epochs. The batch size for all models was determined out of the memory constraints.

6.6 Results

Overall, a dataset of powdery mildew-infected leaves was collected with the user-grade RGB cameras. A number of neural networks were trained with the best of them performing on par with the human experts. The inference time on the onboard computer is well below the maximal acceptable time, thus leaving room for the introduction of other models or increasing the number of cameras.

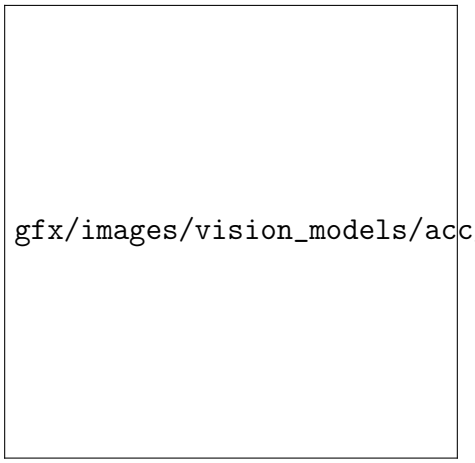

Figure 6-5: Performance and FPS of the models trained on the first dataset with inference on the server.

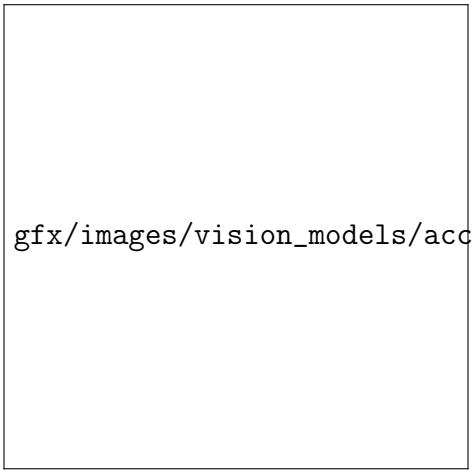

Figure 6-6: Performance and FPS of the chosen best models trained on the first dataset with inference on the onboard laptop.

Table **??** presents the results of the training of all the models considered on the first version of the dataset, see Section **??**. It was not possible to run certain models on the onboard laptop, taking into account the target resolution of 1056 $\times$ 1056. These models are marked with a dash sign in the *Onboard PC inference* column. These models were excluded from further experiments because they were too demanding in terms of computational resources.

All the models were examined from the standpoint of the combination of accuracy and inference time, see Figure **??** for the results on the server. It turns out, that three of them are Pareto-optimal, meaning that no other model is faster and more precise at the same time. Those are YOLOv8n, MobilenetV3small

and MobilenetV3large. Figure **??** gives their results on the target machine.

Another series of experiments was carried out with three aforementioned models and the second version of the dataset, see Table **??**. The results did not subvert the expectations with accuracy slightly increasing for MobilenetV3small and slightly dropping for other models.

With the third version of the dataset the accuracy values have become significantly worse, see Table **??**. The values of the metrics for different models are relatively close to each other, matching the consistency of the experts in terms of accuracy. Thus, the reasonable qualitative explanation could be that the performance is limited more or less by the data quality, not the models' generalization capabilities. The best performance by both accuracy and time was shown by YOLOv8n neural network. The False Negative rate for it is 6 %.

In order to assess the model performance on the high-quality data, a set of 100 images was labeled by a consensus of 4 experts. The consensus here means that the image-wise labels were agreed upon by all the experts. The output of the model matched the expert labeling for 96 samples of 100.

The overall performance in terms of speed is well above the minimal requirements, meaning that the monitoring speed is limited by the robot's motion (because of safety concerns), not by the inference time of the neural networks.

It is worth noting that this excessive performance could be beneficial for solving other related problems. For instance, to detect certain tiny insects it will be necessary to install much more cameras with small FoV. Their number could rise to dozens, requiring very low inference time for a single image. These cases could be addressed without any substantial modification to the vision pipeline.

6.7 Conclusion and future work

6.7.1 Conclusion

An autonomous agricultural robot on an omnidirectional platform was designed, prototyped, and tested in a real environment. The camera's positioning allows for the examination of the whole tomato plant, and the onboard computer is capable of processing the data in real-time.

A dataset of powdery mildew-infected tomato leaves was collected, labeled and assessed in terms of consistency. It contains a sufficient amount of data for training modern neural networks of reasonable size, which makes it useful for further industrial applications.

Several modern neural networks were trained for classification and compared on two test sets with one of them being marked by a consensus of experts. The performance of the models is sufficient and matches with the mutual consistencies of the human experts.

It was demonstrated that real-time disease recognition could be performed on the robot while moving with the means of the user-grade cameras. The main limitation of the chosen approach is that RGB cameras require sufficient lighting to function properly. However, in the given circumstances this requirement is naturally met.

6.7.2 Future work

The next steps in this project are planned to be the following. First, the robot requires certain polishing and finalization in terms of mechanics. In order for it to be constantly deployed in a humid environment it should be watertight. On the other hand, isolating the inner volume from the environment will require heat dissipation to be reconsidered.

Second, the cameras are supposed to be substituted by a global shutter-based one. It will practically eliminate the motion blur while requiring certain mod-

ifications to the data transfer subsystem. Moreover, the production-ready version of the camera poles has to be manufactured. It is supposed to hold the cameras with the help of a mechanism that allows for vertical and horizontal position adjustment.

Third, high-level control should be implemented in the system for the robot to be capable of localizing itself and autonomously following the trajectory set by the user.

Fourth, a Graphical User Interface should be implemented for the end user to control the robot without substantial UNIX knowledge.

Finally, more disease types and crop types should be introduced into the vision subsystem.

Markers	A	B	C	D
A	1.0	0.72	0.88	0.82
B		1.00	**0.60**	0.90
C			1.00	**0.70**
D				1.00

1 iteration

Markers	A	B	C	D
A	1.0	0.88	**0.68**	0.96
B		1.00	0.80	0.92
C			1.00	0.72
D				1.00

2 iteration

Markers	A	B	C	D
A	1.0	0.92	0.86	0.90
B		1.00	0.94	0.98
C			1.00	0.96
D				1.00

3 iteration

Markers	A	B	C	D
A	1.0	0.94	0.92	0.92
B		1.00	0.89	0.86
C			1.00	0.92
D				1.00

4 iteration

Table 6.1: Tables of mutual consistencies of the human experts. Each table represents one of 4 iterations of the data markup. The consistencies of 0.7 and below are highlighted in bold. A, B, C, and D in the tables represent individual human experts. The number in ij-th element of the table is the fraction of the matching labels (positive or negative) for the corresponding experts on a subset of 50 images that they shared during that iteration. The mean consistency (excluding the consistency of the experts with themselves) is 0.8579, which closely matches the accuracy of the best model.

Model	Params	Accuracy [%]	Server inference[ms]	Onboard PC inference[ms]	Training time	Epochs
Resnet34	21.8M	84.40	34.7	38.23	169m 40s	40
Resnet152	60.2M	85.40	34.00	-	96m 58s	40
YOLOv8n	3.2M	**85.80**	5.9	**6.6**	25m 54s	30
YOLOv8s	11.2M	85.00	10.6	12.5	27m 37s	30
YOLOv8m	25.9M	84.50	30.7	33.0	29m 40s	30
EfficientNetV2	18.5M	84.07	49.3	-	124m 19s	40
EfficientNetB3	12.2M	80.53	14.86	-	66m 45s	40
EfficientNetB4	19.3M	79.20	19.7	-	74m 29s	40
MobilenetV3small	2.5M	83.63	4.15	6.64	54m 23s	40
MobilenetV3large	5.5M	84.51	4.81	19.21	52m 23s	40

Table 6.2: The performance of all models on the first dataset.

Model	Accuracy	Inference server (ms)	Inference (ms)	Training time	Epochs	Batch
YOLOv8n	85.4	5.9	6.6	83m 52s	40	16
MobilenetV3small	84.17	4.2	6.61	182m 59s	40	32
MobilenetV3large	82.74	4.87	19.41	357m 19s	40	32

Table 6.3: The performance of the selected models on the second dataset.

Model	Accuracy	Inference server (ms)	Inference (ms)	Training time	Epochs	Batch
YOLOv8n	77.5	3.3	7.3	472m 32s	40	16
MobilenetV3small	77.45	4.08	6.65	293m 1s	40	16
MobilenetV3large	77.45	4.95	19.16	321m 32s	40	16

Table 6.4: The performance of the selected models on the third dataset.

"If you optimize everything, you will always be unhappy."

Donald Knuth

Chapter 7

Conclusion

In this last chapter, we discuss the results, the limitations of our work, and provide an outlook on future work.

Glossary

SK Skolkovo Institute of Science and Technology. 12, 16, 21, 77

SysML Systems Modeling Language. 14

Bibliography

Amaresh Chakrabarti and Lucienne T. M. Blessing, editors. *An Anthology of Theories and Models of Design*. Springer London, London, 2014. ISBN 978-1-4471-6337-4. doi:10.1007/978-1-4471-6338-1. URL http://link.springer.com/10.1007/978-1-4471-6338-1.

Object Management Group. OMG Systems Modeling Language (SysML) 1.4, 2015. URL https://www.omg.org/spec/SysML/1.4/.

Skoltech. CEDESK - Concurrent Engineering Data Exchange Skoltech, 2017. URL https://cedesk.github.io/.

Appendix A

Additional Resources

?? contains some additional material.

Feature	**Method X**	**Method Y**	**References**
Speed	medium	slow	**?**
Cost	less	more	
Error	2	3	

Table A.1: Comparison of X and Y